

In light of the anonymous reviews, please find below our responses to the raised issues.

First, we would like to gratefully thank the reviewers for their work in reading and reviewing the manuscript. Please know that all the proposed changes have been made to the manuscript.

In response to anonymous referee #1.

We have adjusted and clarified issues in the introduction related the description of the process and the terminology related to the initiation.

1 Towards a model for structured mass movements: the
2 **OpenLISEM Hazard model 2.0a**

3 Bastian van den Bout*¹ Theo van Asch² Wei Hu² Chenxiao X. Tang³ Olga Mavrouli¹ Victor G.Jetten¹ CeesJ.
4 van Westen¹

5 ¹University of Twente, Faculty of Geo-Information Science and Earth Observation

6 ²Chengdu university of Technology, State key Laboratory of Geohazard Prevention and GeoEnvironment
7 Protection

8 ³Institute of Mountain Hazards and Environment, Chinese Academy of Sciences

9 *Correspondence to:* Bastian van den Bout (b.vandenbout@utwente.nl)

10

11 **Abstract**

12 Mass movements such as debris flows and landslides differ in behavior due to their material properties and
13 internal forces. Models employ generalized multi-phase flow equations to adaptively describe these complex
14 flow types. Such models commonly assume unstructured and fragmented flow, where internal cohesive strength
15 is insignificant. In this work, existing work on two-phase mass movement equations are extended to include a
16 full stress-strain relationship that allows for runout of (semi-) structured fluid-solid masses. The work provides
17 both the three-dimensional equations and depth-averaged simplifications. The equations are implemented in a
18 hybrid Material Point Method (MPM) which allows for efficient simulation of stress-strain relationships on
19 discrete smooth particles. Using this framework, the developed model is compared to several flume experiments
20 of clay blocks impacting fixed obstacles. Here, both final deposit patterns and fractures compare well to
21 simulations. Additionally, numerical tests are performed to showcase the range of dynamical behavior produced
22 by the model. Important processes such as fracturing, fragmentation and fluid release are captured by the model.
23 While this provides an important step towards complete mass movement models, several new opportunities arise
24 such as application to fragmenting mass movements and block-slides.

25

26 **1. Introduction**

27 The earths rock cycle involves sudden release and gravity-driven transport of sloping materials. These
28 mass movements have a significant global impact in financial damage and casualties (Nadim et al., 2006;
29 Kjekstad & Highland, 2009). Understanding the physical principles at work at their initiation and runout phase
30 allows for better mitigation and adaptation to the hazard they induce (Corominas et al., 2014). Many varieties of
31 gravitationally-driven mass movements have been categorized according to their material physical parameters
32 and type of movement. Examples are slides, flows and falls consisting of soil, rocks or debris (Varnes, 1987).
33 Major factors in determining the dynamics of mass movement runout are the composition of the moving material
34 and the internal and external forces during initiation and runout.

35 Within the cluster of existing mass movement processes, a distinction can be made based on the
36 cohesive of the mass during movement. Post-release, a sloping mass might be unstructured, such as mud flows,
37 where grain-grain cohesive strength is absent. Alternatively, the mass can be fragmentative, such as strongly-
38 deforming landslides or fragmenting of rock avalanches upon particle impacts. Finally, there are
39 coherent/structured mass movements, such as can be the case in block-slides where internal cohesive strength
40 can resist deformation for some period (Varnes, 1987). The general importance of the initially structured nature
41 of mass movement material is observed for a variety of reasons. First, block slides are an important subset of
42 mass movement types (Hayir, 2003; Beutner et al., 2008; Tang et al., 2008). This type of mass movement
43 features some cohesive structure to the dynamic material in the movement phase. Secondly, during movement,
44 the spatial gradients in local acceleration induce strain and stress that results in fracturing. This process, often
45 called fragmentation in relation to structured mass movements, can be of crucial importance for mass movement
46 dynamics (Davies & McSaveney, 2009; Delaney & Evans, 2014; Dufresne et al., 2018; Corominas et al. 2019).
47 Lubricating effect from basal fragmentation can enhance velocities and runout distance significantly (Davies et
48 al., 2006; Tang et al., 2009). Otherwise, fragmentation generally influences the rheology of the movement by
49 altering grain-grain interactions (Zhou et al., 2005). The importance of structured material dynamics is further
50 indicated by engineering studies on rock behavior and fracture models (Kaklauskas & Ghaboussi, 2001; Ngekepe
51 et al., 2016; Dhanmeher, 2017).

52 Dynamics of geophysical flows are complex and depend on a variety of forces due to their multi-phase
53 interactions (Hutter et al., 1996). Physically-based models attempt to describe the internal and external forces of
54 all these mass movements in a generalized form (David & Richard, 2011; Pudasaini, 2012; Iverson & George,
55 2014). This allows these models to be applied to a wide variety of cases, while improving predictive range. A
56 variety of both one, two and three- dimensional sets of equations exist to describe the advection and forces that
57 determine the dynamics of geophysical flows.

58 For unstructured (fully fragmented) mass movements, a variety of models exist relating to mohr-
59 coulomb mixture theory. [Such mass movements are described as non-Newtonian granular flows with dominant
60 particle-particle interactions, assuming perfect mixing and continuous movement. Examples are debris flows and
61 mudslides, while block-slides and rockslides do not fit these criteria. Within these models, the Mohr-Coulomb
62 failure surface is described with zero cohesive strength, and only an internal friction angle \(Pitman & Le, 2005\).](#)
63 Examples that simulated a single mixed material (Rickenmann et al., 2006; O'Brien et al., 2007; Luna et al.,
64 2012; van Asch et al., 2014). Two phase models describe both solids, fluids and their interactions and provide
65 additional detail and generalize in important ways (Sheridan et al., 2005; Pitman & Le, 2005; Pudasaini,
66 2012; George & Iverson, 2014; Mergili et al., 2017). Recently, a three-phase model has been developed that
67 includes the interactions between small and larger solid phases (Pudasaini & Mergili, 2019). Typically,
68 implemented forces include gravitational forces and, depending on the rheology of the equations, drag forces,
69 viscous internal forces and a plasticity-criterion. The assumption of [zero cohesion in the Mohr-Coulomb
70 materialunstructured-flow](#) is invalid for any structured mass movement. Some models do implement a non-
71 Newtonian viscous yield stress based on depth-averaged strain estimations (Boetticher et al., 2016; Fornes et al.,
72 2017; Pudasaini & Mergili, 2019). However, this approach lacks the process of fragmentation and internal
73 failure.

74 For structured mass movements, ~~with particle-particle cohesive strength,~~ limited approaches are
75 available. [These movements feature some discrete inter-particle connectivity that allows the moving material to
76 maintain an elasto-plastic structure. Examples here are block-slides rock-slides and some landslides \(Aaron &
77 Hungr, 2016\). These materials can be described by a Mohr-Coulomb material with cohesive strength \(Spencer,
78 2004\).](#) Aaron & Hungr developed a model for simulation of initially coherent rock avalanches (Aaron & Hungr,
79 2016) as part of DAN3D Flex. Within their approach, a rigid-block momentum analysis is used to simulate
80 initial movement of the block. After a specified time, the block is assumed to fragment, and a granular flow
81 model using a Voellmy-type rheology is used for further runout. Their approach thus lacks a physical basis for
82 the fragmenting behavior. Additionally, by dissecting the runout process in two stages (discrete block and
83 granular flow), benefits of holistic two-phase generalized runout models are lost. Finally, Greco et al. (2019)

84 presented a runout model for cohesive granular matrix. Their approach similarly lacks a description of the
85 fragmentation process. Thus, within current mass movement models, there might be improvements available
86 from assuming non-fragmented movement. This would allow for description of structured mass movement
87 dynamics.

88 In this paper, a generalized mass movement model is developed to describe runout of an arbitrarily
89 structured two-phase Mohr-Coulomb material. The model extends on recent innovations in generalized models
90 for mohr-coulomb mixture flow (Pudasaini, 2012; Pudasaini & Mergili, 2019). The second section of this work
91 provides the derivation of the extensive set of equations that describe structured mass movements in a
92 generalized manner. The third section validates the developed model by comparison with results from controlled
93 flume runout experiments. Additionally, this section shows numerical simulation examples that highlight
94 fragmentation behavior and its influence on runout dynamics. Finally, in section four, a discussion on the
95 potential usage of the presented model is provided together with reflection on important opportunities of
96 improvement.

97 2. A set of mass movement equations incorporating internal structure

98 2.1 Structured mass movements

99 ~~Initiation of g~~Gravitational mass flows ~~occurs when~~ are triggered when local the driving forces within a
100 ~~often steep, section of a slope exceed a critical threshold. -sloping material is released.~~ The instability of such
101 materials is generally understood to take place along a failure plane (Zhang et al., 2011, Stead & Wolter, 2015).
102 Along this plane, forces exerted due to gravity and possible seismic accelerations can act as a driving force
103 towards the downslope direction, while a normal-force on the terrain induces a resisting force (Xie et al., 2006).
104 When internal stress exceeds a specified criteria, commonly described using Mohr-Coulomb theory, fracturing
105 occurs, and the material becomes dynamic. Observations indicate material can initially fracture predominantly at
106 the failure plane (Tang et al., 2009 Davies et al., 2006). Full finite-element modelling of stability confirms no
107 fragmentation occurs at initiation, and runout can start as a structured mass (Matsui & San, 1992; Griffiths &
108 Lane, 1999).

109 Once movement is initiated, the material is accelerated. Due to spatially non-homogeneous acceleration,
110 either caused by a non-homogeneous terrain slope, or impact with obstacles, internal stress can build within the
111 moving mass. The stress state can reach a point outside the yield surface, after which some form of deformation
112 occurs (e.g. Plastic, Brittle, ductile) (Loehnert et al., 2008). In the case of rock or soil material, elastic/plastic
113 deformation is limited and fracturing occurs at relatively low strain values (Kaklauskas & Ghaboussi, 2001;
114 Dhanmeher., 2017). Rocks and soil additionally show predominantly brittle fracturing, where strain increments
115 at maximum stress are small (Bieniawski, 1967; Price, 2016; Husek et al., 2016). For soil matrices, cohesive
116 bonds between grains originate from causes such as cementing, frictional contacts and root networks (Cohen et
117 al., 2009). Thus, the material breaks along either the grain-grain bonds or on the molecular level. In practice, this
118 processes of fragmentation has been both observed and studied frequently. Cracking models for solids use stress-
119 strain descriptions of continuum mechanics (Menin et al., 2009; Ngekpe et al., 2016). Fracture models frequently
120 use Smooth Particle Hydrodynamics (SPH) since a Lagrangian, meshfree solution benefits possible fracturing
121 behavior (Maurel & Combescur, 2008; Xu et al., 2010; Osorno & Steeb, 2017). Within the model developed
122 below, knowledge from fracture-simulating continuum mechanical models is combined with finite element fluid
123 dynamic models.

124 The mohr-coulomb mixture models on which the developed model is based, can be found in Pitman &
125 Le (2005), Pudasaini (2012), George & Iverson, 2014 and Pudasaini & Mergili (2019). While these are
126 commonly names debris-flow models, their validity extends beyond this typical category of mass movement.
127 This is both apparent from model applications (Mergili et al., 2018) and theoretical considerations (Pudasaini,
128 2012). A major cause for the usage of debris flow as a term here is the assumption of unstructured flow, which
129 we are aiming to solve in this work.

130 2.2 Model description

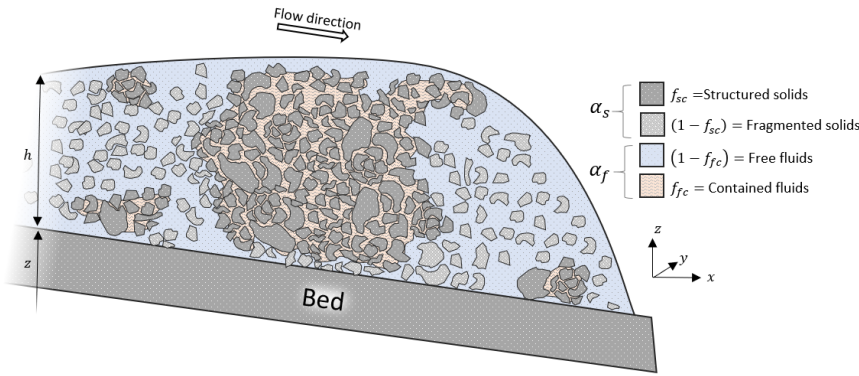
131 We define two phases, solids and fluids, within the flow, indicated by s and f respectively. A specified
132 fraction of solids within this mixture is at any point part of a structured matrix. This structured solid phase,
133 indicated by sc envelops and confines a fraction of the fluids in the mixture, indicates as fc . The solids and
134 fluids are defined in terms of the physical properties such as densities (ρ_f, ρ_s) and volume fractions ($\alpha_f =$
135 $\frac{f}{f+s}, \alpha_s = \frac{s}{f+s}$). The confined fractions of their respective phases are indicated as f_{sc} and f_{fc} for the volume
136 fraction of confined solids and fluids respectively (Equations 1,2 and 3).

137 1. $\alpha_s + \alpha_f = 1$

$$138 \quad 2. \quad \alpha_s(f_{sc} + (1 - f_{sc})) + \alpha_f(f_{fc} + (1 - f_{fc})) = 1$$

$$139 \quad 3. \quad (f_{sc} + (1 - f_{sc})) = (f_{fc} + (1 - f_{fc})) = 1$$

140 For the solids, additionally internal friction angle (ϕ_s) and effective (volume-averaged) material size
 141 (d_s) are defined. We additionally define $\alpha_c = \alpha_s + f_{fc}\alpha_f$ and $\alpha_u = (1 - f_{fc})\alpha_f$ to indicate the solids with
 142 confined fluids and free fluid phases respectively. These phases have a volume-averaged density ρ_{sc}, ρ_f . We let
 143 the velocities of the unconfined fluid phase ($\alpha_u = (1 - f_{fc})\alpha_f$) be defined as $\mathbf{u}_u = (u_u, v_u)$. We assume
 144 velocities of the confined phases ($\alpha_c = \alpha_s + f_{fc}\alpha_f$) can validly be assumed to be identical to the velocities of
 145 the solid phase, $\mathbf{u}_c = (u_c, v_c) = \mathbf{u}_s = (u_s, v_s)$. A schematic depiction of the represented phases is shown in
 146 Figure 1.



147
 148 *Figure 1 A schematic depiction of the flow contents. Both structured and unstructured solids are*
 149 *present. Fluids can be either free, or confined by the structured solids.*

150 A major assumption is made here concerning the velocities of both the confined and free solids (sc and
 151 s), that have a shared averaged velocity (\mathbf{u}_s). We deliberately limit the flow description to two phases, opposed
 152 to the innovative work of Pudasaini & Mergili (2019) that develop a multi-mechanical three-phase model. This
 153 choice is motivated by considerations of applicability (reducing the number of required parameters), the infancy
 154 of three-phase flow descriptions and finally the general observations of the validity of this assumption (Ishii,
 155 1975; Ishii & Zuber, 1979; Drew, 1983; Jakob et al, 2005; George & Iverson, 2016).

156 The movement of the flow is described initially by means of mass and momentum conservation
 157 (Equations 4 and 5).

$$158 \quad 4. \quad \frac{\partial \alpha_c}{\partial t} + \nabla \cdot (\alpha_c \mathbf{u}_c) = 0$$

$$159 \quad 5. \quad \frac{\partial \alpha_u}{\partial t} + \nabla \cdot (\alpha_u \mathbf{u}_u) = 0$$

160 Here we add the individual forces based on the work of Pudasaini & Hutter (2003), Pitman & Le
 161 (2005), Pudasaini (2012), Pudasaini & Fischer (2016) and Pudasaini & Mergili (2019) (Equations 6 and 7).

$$162 \quad 6. \quad \frac{\partial}{\partial t} (\alpha_c \rho_c \mathbf{u}_c) + \nabla \cdot (\alpha_c \rho_c \mathbf{u}_c \otimes \mathbf{u}_c) = \alpha_c \rho_c \mathbf{f} - \nabla \cdot \alpha_c \mathbf{T}_c + p_c \nabla \alpha_c + \mathbf{M}_{DG} + \mathbf{M}_{vm}$$

$$163 \quad 7. \quad \frac{\partial}{\partial t} (\alpha_u \rho_f \mathbf{u}_u) + \nabla \cdot (\alpha_u \rho_f \mathbf{u}_u \otimes \mathbf{u}_u) = \alpha_u \rho_f \mathbf{f} - \nabla \cdot \alpha_u \mathbf{T}_u + p_f \nabla \alpha_u - \mathbf{M}_{DG} - \mathbf{M}_{vm}$$

164 Where \mathbf{f} is the body force (among which is gravity), \mathbf{M}_{DG} is the drag force, \mathbf{M}_{vm} is the virtual mass
 165 force and $\mathbf{T}_c, \mathbf{T}_u$ are the stress tensors for solids with confined fluids and unconfined phases respectively. The
 166 virtual mass force described the additional work required by differential acceleration of the phases. The drag
 167 force describes the drag along the interfacial boundary of fluids and solids. The body force describes external
 168 forces such as gravitational acceleration and boundary forces. Finally, the stress tensors describe the internal
 169 forces arising from strain and viscous processes. Both the confined and unconfined phases in the mixture are
 170 subject to stress tensors (\mathbf{T}_c , and \mathbf{T}_u), for which the gradient acts as a momentum source. Additionally, we follow
 171 Pudasaini (2012) and add a buoyancy force ($p_c \nabla \alpha_c$ and $p_f \nabla \alpha_u$).

172 **Stress Tensors, Describing internal structure**

173 Based on known two-phase mixture theory, the internal and external forces acting on the moving
 174 material are now set up. This results in several unknowns such as the stress tensors (\mathbf{T}_c and \mathbf{T}_u , described by the
 175 constitutive equation), the body force (\mathbf{f}), the drag force (\mathbf{M}_{DG}) and the virtual mass force (\mathbf{M}_{VM}). This section
 176 will first describe the derivation of the stress tensors. These describe the internal stress and viscous effects. To
 177 describe structured movements, these require a full stress-strain relationship which is not present in earlier
 178 generalized mass movements model. Afterwards, existing derivation of the body, drag and virtual mass force are
 179 altered to conform the new constitutive equation.

180 Our first step in defining the momentum source terms in equations 6 and 7 is the definition of the fluid
 181 and solid stress tensors. Current models typically follow the assumptions made by Pitman & Le (2005), who
 182 indicate: “*Proportionality and alignment of the tangential and normal forces are imposed as a basal boundary
 183 condition is assumed to hold throughout the layer of flowing material ... following Rankine (1857) and Terzaghi
 184 (1936), an earth pressure relation is assumed for diagonal stress components*”. Here, the earth pressure
 185 relationship is a vertically-averaged analytical solution for lateral forces exerted by an earth wall. Thus,
 186 unstructured columns of moving mixtures are assumed. Here, we aim to use the full Mohr-Coulomb relations.
 187 Describing the internal stress of soil and rock matrices is commonly achieved by elastic-plastic simulations of
 188 the materials stress-strain relationship. Since we aim to model a full stress description, the stress tensor is equal
 189 to the elasto-plastic stress tensor (Equation 8).

190 8. $\mathbf{T}_c = \boldsymbol{\sigma}$

191 Where $\boldsymbol{\sigma}$ is the elasto-plastic stress tensor for solids. The stress can be divided into the deviatoric and
 192 non-deviatoric contributions (Equation 9). The non-deviatoric part acts normal on any plane element (in the
 193 manner in which a hydrostatic pressure acts equal in all directions). Note that we switch to tensor notation when
 194 describing the stress-strain relationship. Thus, superscripts (α and β) represent the indices of basis vectors (x, y
 195 or z axis in Euclidian space), and obtain tensor elements. Additionally, the Einstein convention is followed
 196 (automatic summation of non-defined repeated indices in a single term).

197 9. $\sigma^{\alpha\beta} = s^{\alpha\beta} + \frac{1}{3}\sigma^{\gamma\gamma}\delta^{\alpha\beta}$

198 Where s is the deviatoric stress tensor and $\delta^{\alpha\beta} = [\alpha = \beta]$ is the Kronecker delta.

199 Here, we define the elasto-plastic stress (σ) based on a generalized Hooke-type law in tensor notation
 200 (Equation 10 and 11) where plastic strain occurs when the stress state reaches the yield criterion (Spencer, 2004;
 201 Necas & Hlavecek, 2007; Bui et al., 2008).

202 10. $\dot{\epsilon}_{elastic}^{\alpha\beta} = \frac{\dot{s}^{\alpha\beta}}{2G} + \frac{1-2\nu}{E}\dot{\sigma}^m\delta^{\alpha\beta}$

203 11. $\dot{\epsilon}_{plastic}^{\alpha\beta} = \dot{\lambda}\frac{\partial g}{\partial \sigma^{\alpha\beta}}$

204 Where $\dot{\epsilon}_{elastic}$ is the elastic strain tensor, $\dot{\epsilon}_{plastic}$ is the plastic strain tensor, $\dot{\sigma}^m$ is the mean stress rate
 205 tensor, ν is Poisson’s ratio, E is the elastic Young’s Modulus, G is the shear modulus, \dot{s} is the deviatoric shear
 206 stress rate tensor, $\dot{\lambda}$ is the plastic multiplier rate and g is the plastic potential function. Additionally, the strain
 207 rate is defined from velocity gradients as equation 12.

208 12. $\dot{\epsilon}_{total}^{\alpha\beta} = \dot{\epsilon}_{elastic}^{\alpha\beta} + \dot{\epsilon}_{plastic}^{\alpha\beta} = \frac{1}{2}\left(\frac{\partial u_x^\alpha}{\partial x^\beta} - \frac{\partial u_x^\beta}{\partial x^\alpha}\right)$

209 By solving equations 9, 10 and 11 for $\dot{\sigma}$, a stress-strain relationship can be obtained (Equation 13) (Bui
 210 et al., 2008).

211 13. $\dot{\sigma}^{\alpha\beta} = 2G\dot{\epsilon}^{\gamma\gamma}\delta^{\alpha\beta} + K\dot{\epsilon}^{\gamma\gamma}\delta^{\alpha\beta} - \dot{\lambda}\left[\left(K - \frac{2G}{3}\right)\frac{\partial g}{\partial \sigma^{mn}}\delta^{mn}\delta^{\alpha\beta} + 2G\frac{\partial g}{\partial \sigma^{\alpha\beta}}\right]$

212 Where $\dot{\epsilon}$ is the deviatoric strain rate ($\dot{\epsilon}^{\alpha\beta} = \dot{\epsilon}^{\gamma\gamma} - \frac{1}{3}\dot{\epsilon}^{\alpha\beta}\delta^{\alpha\beta}$), ψ is the dilatancy angle and K is the
 213 elastic bulk modulus and the material parameters defined from E and ν (Equation 14).

214 14. $K = \frac{E}{3(1-2\nu)}, G = \frac{E}{2(1+\nu)}$

215 Fracturing or failure occurs when the stress state reaches the yield surface, after which plastic
 216 deformation occurs. The rate of change of the plastic multiplier specifies the magnitude of plastic loading and
 217 must ensure a new stress state conforms to the conditions of the yield criterion. By means of substituting

218 equation 13 in the consistency condition ($\frac{\partial f}{\partial \sigma^{\alpha\beta}} d\sigma^{\alpha\beta} = 0$), the plastic multiplier rate can be defined (Equation
219 15) (Bui et al., 2008).

$$220 \quad 15. \quad \dot{\lambda} = \frac{2G\epsilon^{\alpha\beta} \frac{\partial f}{\partial \sigma^{\alpha\beta}} + (K - \frac{2G}{3}) \dot{\epsilon}^{\gamma\gamma} \frac{\partial f}{\partial \sigma^{\alpha\beta}} \sigma^{\alpha\beta} \delta^{\alpha\beta}}{2G \frac{\partial f}{\partial \sigma^{mn}} \frac{\partial g}{\partial \sigma^{mn}} + (K - \frac{2G}{3}) \frac{\partial f}{\partial \sigma^{mn}} \delta^{mn} \frac{\partial g}{\partial \sigma^{mn}} \delta^{mn}}$$

221 The yield criteria specifies a surface in the stress-state space that the stress state can not pass, and at
222 which plastic deformation occurs. A variety of yield criteria exist, such as Mohr-Coulomb, Von Mises, Ducker-
223 Prager and Tresca (Spencer, 2004). Here, we employ the Ducker-Prager model fitted to Mohr-Coulomb material
224 parameters for its accuracy in simulating rock and soil behavior, and numerical stability (Spencer, 2004; Bui et
225 al., 2008) (Equation 16 and 17).

$$226 \quad 16. \quad f(I_1, J_2) = \sqrt{J_2} + \alpha_\phi I_1 - k_c = 0$$

$$227 \quad 17. \quad g(I_1, J_2) = \sqrt{J_2} + \alpha_\phi I_1 \sin(\psi)$$

228 Where I_1 and J_2 are tensor invariants (Equation 18 and 19).

$$229 \quad 18. \quad I_1 = \sigma^{xx} + \sigma^{yy} + \sigma^{zz}$$

$$230 \quad 19. \quad J_2 = \frac{1}{2} s^{\alpha\beta} s^{\alpha\beta}$$

231 Where the Mohr-Coulomb material parameters are used to estimate the Ducker-Prager parameters
232 (Equation 20).

$$233 \quad 20. \quad \alpha_\phi = \frac{\tan(\phi)}{\sqrt{9+12 \tan^2 \phi}}, \quad k_c = \frac{3c}{\sqrt{9+12 \tan^2 \phi}}$$

234 Using the definitions of the yield surface and stress-strain relationship, combining equations 13, 15, 16
235 and 17, the relationship for the stress rate can be obtained (Equation 21 and 22).

$$236 \quad 21. \quad \dot{\sigma} = 2G \dot{\epsilon}^{\alpha\beta} + K \dot{\epsilon}^{\gamma\gamma} \delta^{\alpha\beta} - \dot{\lambda} \left[9K \sin \psi \delta^{\alpha\beta} + \frac{G}{\sqrt{J_2}} s^{\alpha\beta} \right]$$

$$237 \quad 22. \quad \dot{\lambda} = \frac{3\alpha K \dot{\epsilon}^{\gamma\gamma} + \left(\frac{G}{\sqrt{J_2}} \right) s^{\alpha\beta} \dot{\epsilon}^{\alpha\beta}}{27\alpha_\phi K \sin \psi + G}$$

238 In order to allow for the description of large deformation, the Joumann stress rate can be used, which is
239 a stress-rate that is independent from a frame of reference (Equation 23).

$$240 \quad 23. \quad \hat{\sigma} = \sigma^{\alpha\gamma} \dot{\omega}^{\beta\gamma} + \sigma^{\gamma\beta} \dot{\omega}^{\alpha\gamma} + 2G \dot{\epsilon}^{\alpha\beta} + K \dot{\epsilon}^{\gamma\gamma} \delta^{\alpha\beta} - \dot{\lambda} \left[9K \sin \psi \delta^{\alpha\beta} + \frac{G}{\sqrt{J_2}} s^{\alpha\beta} \right]$$

241 Where $\dot{\omega}$ is the spin rate tensor, as defined by equation 24.

$$242 \quad 24. \quad \dot{\omega}^{\alpha\beta} = \frac{1}{2} \left(\frac{\partial v^\alpha}{\partial x^\beta} - \frac{\partial v^\beta}{\partial x^\alpha} \right)$$

243 Due to the strain within the confined material, the density of the confined solid phase (ρ_c) evolves
244 dynamically according to equation 25.

$$245 \quad 25. \quad \rho_c = f_{sc} \rho_s \frac{\epsilon_v}{\epsilon_v} + (1 - f_{sc}) \rho_s + f_{fc} \rho_f$$

246 Where ϵ_v is the total volume strain, $\epsilon_v \approx \epsilon_1 + \epsilon_2 + \epsilon_3$, ϵ_i is one of the principal components of the
247 strain tensor. Since we aim to simulate brittle materials, where volume strain remains relatively low, we assume
248 that changes in density are small compared to the original density of the material ($\frac{\partial \rho_c}{\partial t} \ll \rho_c$).

249 Fragmentation

250 Brittle fracturing is a processes commonly understood to take place once a material internal stress has
251 reached the yield surface, and plastic deformation has been sufficient to pass the ultimate strength point (Maurel
252 & Cumescore, 2008; Husek et al., 2016). A variety of approaches to fracturing exist within the literature (Ma et
253 al., 2014; Osomo & Steeb, 2017). FEM models use strain-based approaches (Loehnert et al., 2008). For SPH
254 implementations, as will be presented in this work, distance-based approaches have provided good results
255 (Maurel & Cumescore, 2008). Other works have used strain-based fracture criteria (Xu et al., 2010) .
256 Additionally, dynamic degradation of strength parameters have been implemented (Grady & Kipp, 1980; Vuyst
257 & Vignjevic, 2013; Williams, 2019). Comparisons with observed fracture behavior has indicated the predictive
258 value of these schemes (Xu et al., 2010; Husek et al., 2016). We combine the various approaches to best fit the
259 dynamical multi-phase mass movement model that is developed. Following, Grady & Kipp (1980) and we

260 simulate a degradation of strength parameters. Our material consists of a soil and rock matrix. We assume
 261 fracturing occurs along the inter-granular or inter-rock contacts and bonds (see also Cohen et al., 2009). Thus,
 262 cohesive strength is lost for any fractured contacts. We simulate degradation of cohesive strength according to a
 263 volume strain criteria. When the stress state lies on the yield surface (the set of critical stress states within the 6-
 264 dimensional stress-space), during plastic deformation, strain is assumed to attribute towards fracturing. A critical
 265 volume strain is taken as material property, and the breaking of cohesive bonds occurs based on the relative
 266 volume strain. Following Grady & Kipp (1980) and Vuyst & Vignjevic (2013), we assume that the degradation
 267 behavior of the strength parameter is distributed according to a probability density distribution. Commonly, a
 268 Weibull-distribution is used (Williams, 2019). Here, for simplicity, we use a uniform distribution of cohesive
 269 strength between 0 and $2c_0$, although any other distribution can be substituted. Thus, the expression governing
 270 cohesive strength becomes equation 26

$$271 \quad 26. \quad \frac{\partial c}{\partial t} = \begin{cases} -c_0 \frac{1}{2} \frac{\left(\frac{\epsilon_v}{\epsilon_{v0}}\right)}{\epsilon_c} & f(I_1, J_2) \geq 0, c > 0 \\ 0 & \text{otherwise} \end{cases}$$

272 Where c_0 is the initial cohesive strength of the material, ϵ_{v0} is the initial volume, $\left(\frac{\epsilon_v}{\epsilon_{v0}}\right)$ is the fractional
 273 volumetric strain rate, ϵ_c is the critical fractional volume strain for fracturing.

274 Water partitioning

275 During the movement of the mixed mass, the solids can thus be present as a structured matrix. Within
 276 such a matrix, a fluid volume can be contained (e.g. as originating from a ground water content in the original
 277 landslide material). These fluids are typically described as groundwater flow following Darcy's law, which poses
 278 a linear relationship between pressure gradients and flow velocity through a soil matrix. In our case, we assumed
 279 the relative velocity of water flow within the granular solid matrix as very small compared to both solid
 280 velocities and the velocities of the free fluids. As an initial condition of the material, some fraction of the water
 281 is contained within the soil matrix (f_{fc}). Additionally, for loss of cohesive structure within the solid phase, we
 282 transfer the related fraction of fluids contained within that solid structure to the free fluids.

$$283 \quad 27. \quad \frac{\partial f_{fc}}{\partial t} = -\frac{\partial(1-f_{fc})}{\partial t} = \begin{cases} -f_{fc} \frac{c_0 \max(0.0, \epsilon_v)}{c \epsilon_f} & f(I_1, J_2) \geq 0, c > 0 \\ 0 & \text{otherwise} \end{cases}$$

$$284 \quad 28. \quad \frac{\partial f_{sc}}{\partial t} = -\frac{\partial(1-f_{sc})}{\partial t} = \begin{cases} -f_{sc} \frac{c_0 \max(0.0, \epsilon_v)}{c \epsilon_f} & f(I_1, J_2) \geq 0, c > 0 \\ 0 & \text{otherwise} \end{cases}$$

285 Beyond changes in f_{fc} through fracturing of structured solid materials, no dynamics are simulated for
 286 in- or outflux of fluids from the solid-matrix. The initial volume fraction of fluids in the solid matrix defined by
 287 (f_{fc} and s_{fc}) remains constant throughout the simulation. The validity of this assumption can be based on the
 288 slow typical fluid velocities in a solid matrix relative to fragmented mixed fluid-solid flow velocities (Kern,
 289 1995; Saxton and Rawls, 2006). While the addition of evolving saturation would extend validity of the model, it
 290 would require implementation of pretransfer-functions for evolving material properties, which is beyond the
 291 scope of this work. An important note on the points made above is the manner in which fluids are re-partitioned
 292 after fragmentation. All fluids in fragmented solids are released, but this does not equate to free movement of the
 293 fluids or a disconnection from the solids that confined them. Instead, the equations continue to connect the solids
 294 and fluids through drag, viscous and virtual mass forces. Finally, the density of the fragmented solids is assumed
 295 to be the initially set solid density. Any strain-induced density changes are assumed small relative to the initial
 296 solid density ($\frac{\rho_c}{\rho_s} \ll 1$).

297 Fluid Stresses

298 The fluid stress tensor is determined by the pressure and the viscous terms (Equations 29 and 30).
 299 Confined solids are assumed to be saturated and constant during the flow.

$$300 \quad 29. \quad \mathbf{T}_u = P_f \mathbf{I} + \boldsymbol{\tau}_f$$

$$301 \quad 30. \quad \boldsymbol{\tau}_f = \eta_f [\nabla \mathbf{u}_u + (\nabla \mathbf{u}_c)^t] - \frac{\eta_f}{\alpha_u} \mathcal{A}(\alpha_u) (\nabla \alpha_c (\mathbf{u}_u - \mathbf{u}_c) + (\mathbf{u}_c - \mathbf{u}_u) \nabla \alpha_c)$$

302 Where \mathbf{I} is the identity tensor, $\boldsymbol{\tau}_f$ is the viscous stress tensor for fluids, P_f is the fluid pressure, η_f is the
 303 dynamic viscosity of the fluids and \mathcal{A} is the mobility of the fluids at the interface with the solids that acts as a
 304 phenomenological parameter (Pudasaini, 2012).

305 The fluid pressure acts only on the free fluids here, as the confined fluids are moved together with the
 306 solids. In equation 30, the second term is related to the non-Newtonian viscous force induced by gradients in

307 solid concentration. The effect as described by Pudasaini (2012) is induced by a solid-concentration gradient. In
 308 case of unconfined fluids and unstructured solids ($f_{sf} = 1, f_{sc} = 1$). Within our flow description, we see no
 309 direct reason to eliminate or alter this force with a variation in the fraction of confined fluids or structured solids.
 310 We do only consider the interface between solids and free fluids as an agent that induces this effect, and
 311 therefore the gradient of the gradient of the solids and confined fluids ($\nabla(\alpha_s + f_{fc}\alpha_f) = \nabla\alpha_c$) is used instead of
 312 the total solid phase ($\nabla\alpha_s$).

313 Drag force and Virtual Mass

314 Our description of the drag force follows the work of Pudasaini (2012) and Pudasaini (2018), where a
 315 generalized two-phase drag model is introduced and enhanced. We split their work into a contribution from the
 316 fraction of structured solids (f_{sc}) and unconfined fluids ($1 - f_{fc}$) (Equation 31).

$$317 \quad 31. \quad C_{DG} = \frac{f_{sc}\alpha_c\alpha_u(\rho_c - \rho_f)g}{U_{T,c}(\mathcal{G}(Re)) + S_p} (\mathbf{u}_u - \mathbf{u}_c)|\mathbf{u}_u - \mathbf{u}_c|^{j-1} + \frac{(1-f_{sc})\alpha_c\alpha_u(\rho_s - \rho_f)g}{U_{T,uc}(\mathcal{P}\mathcal{F}(Re_p) + (1-\mathcal{P})\mathcal{G}(Re)) + S_p} (\mathbf{u}_u - \mathbf{u}_c)|\mathbf{u}_u - \mathbf{u}_c|^{j-1}$$

318 Where $U_{T,c}$ is the terminal or settling velocity of the structures solids, $U_{T,uc}$ is the terminal velocity of
 319 the unconfined solids, \mathcal{P} is a factor that combines solid- and fluid like contributions to the drag force, \mathcal{G} is the
 320 solid-like drag contribution, \mathcal{F} is the fluid-like drag contribution and S_p is the smoothing function (Equation 32
 321 and 34). The exponent j indicates the type of drag: linear ($j = 0$) or quadratic ($j = 1$).

322 Within the drag, the following functions are defined:

$$323 \quad 32. \quad F = \frac{\gamma}{180} \left(\frac{\alpha_f}{\alpha_s}\right)^3 Re_p, \quad G = \alpha_f^{M(Re_p)-1}$$

$$324 \quad 33. \quad S_p = \left(\frac{\mathcal{P}}{\alpha_c} + \frac{1-\mathcal{P}}{\alpha_u}\right)\mathcal{K}$$

$$325 \quad 34. \quad \mathcal{K} = |\alpha_c\mathbf{u}_c + \alpha_u\mathbf{u}_u| \approx 10 \text{ m s}^{-1}$$

326 Where M is a parameter that varies between 2.4 and 4.65 based on the Reynolds number (Pitman & Le,
 327 2005). The factor \mathcal{P} that combines solid- and fluid like contributions to the drag, is dependent on the volumetric
 328 solid content in the unconfined and unstructured materials ($\mathcal{P} = \left(\frac{\alpha_s(1-f_{sc})}{\alpha_f(1-f_{fc})}\right)^m$ with $m \approx 1$). Additionally we
 329 assume the factor \mathcal{P} , is zero for drag originating from the structured solids. As stated by Pudasaini & Mergili
 330 (2019) "As limiting cases: \mathcal{P} suitably models solid particles moving through a fluid". In our model, the drag
 331 force acts on the unconfined fluid momentum ($u_{uc}\alpha_f(1 - f_{fc})$). For interactions between unconfined fluids and
 332 structured solids, larger blocks of solid structures are moving through fluids that contains solids of smaller size.

333 Virtual mass is similarly implemented based on the work of Pudasaini (2012) and Pudasaini & Mergili
 334 (2019) (Equation 35). The adapted implementation considers the solids together with confined fluids to move
 335 through a free fluid phase.

$$336 \quad 35. \quad C_{VMG} = \alpha_c\rho_u \left(\frac{1}{2} \left(\frac{1+2\alpha_c}{\alpha_u}\right)\right) \left(\left(\frac{\partial u_u}{\partial t} + \mathbf{u}_u \cdot \nabla \mathbf{u}_u\right) - \left(\frac{\partial u_c}{\partial t} + \mathbf{u}_c \cdot \nabla \mathbf{u}_c\right) \right)$$

337 Where $C_{DG} = \frac{1}{2} \left(\frac{1+2\alpha_c}{\alpha_u}\right)$ is the drag coefficient.

338 Boundary conditions

339 Finally, following the work of Iverson & Denlinger (2001), Pitman & Le (2005) and Pudasaini (2012), a
 340 boundary condition is applied to the surface elements that contact the flow (Equation 36).

$$341 \quad 36. \quad |\mathbf{S}| = N \tan(\phi)$$

342 Where N is the normal pressure on the surface element and \mathbf{S} is the shear stress.

343 2.3 Depth-Averaging

344 The majority of the depth-averaging in this works is analogous to the work of Pitman & Le (2005),
 345 Pudasaini (2012) and Pudasaini & Mergili (2019). Depth-averaging through integration over the vertical extent of
 346 the flow can be done based on several useful and often-used assumptions: $\frac{1}{h} \int_0^h x \, dh = \bar{x}$, for the velocities (u_u
 347 and u_c), solid, fluid and confined fractions (α_f , α_s , f_{fc} and f_{sc}) and material properties (ρ_u , ϕ and c). Besides
 348 these similarities and an identical derivation of depth-averaged continuity equations, three major differences
 349 arise.

350 **i)Fluid pressure**

351 Previous implementations of generalized two-phase debris flow equations have commonly assumed hydrostatic
 352 pressure ($\frac{\partial p}{\partial z} = g^z$) (Pitman & Le, 2005; Pudasaini, 2012; Abe & Konagai, 2016). Here we follow this
 353 assumption for the fluid pressure at the base and solid pressure for unstructured material (Equations 37 and 38).

354 37. $P_{b_s,u} = -(1 - \gamma)\alpha_s g^z h$

355 38. $P_{b_u} = -g^z h$

356 Where $\gamma = \frac{\rho_f}{\rho_s}$ is the density ratio (not to be confused with a tensor index when used in superscript) (-).

357 However, larger blocks of structure material can have contact with the basal topography. Due to density
 358 differences, larger blocks of solid structures are likely to move along the base (Pailhia & Pouliquen, 2009;
 359 George & Iverson, 2014). If these blocks are saturated, water pressure propagates through the solid matrix and
 360 hydrostatic pressure is retained. However, in cases of an unsaturated solid matrix that connects to the base,
 361 hydrostatic pressure is not present there. We introduce a basal fluid pressure propagation factor $\mathcal{B}(\theta_{eff}, \bar{d}_{sc}, \dots)$
 362 which describes the fraction of fluid pressure propagated through a solid matrix (with θ_{eff} the effective
 363 saturation, \bar{d}_{sc} the average size of structured solid matrix blocks). This results in a basal pressure equal to
 364 equation 39.

365 39. $P_{b_c} = -(1 - f_{sc})(1 - \gamma) \frac{(1-f_{sc})\alpha_s}{(1-f_{fc})\alpha_f} g^z h - f_{sc}(1 - \gamma)\mathcal{B} \frac{f_{sc}\alpha_s}{(f_{fc})\alpha_f} g^z h$

366 The basal pressure propagation factor (\mathcal{B}) should theoretically depend, similarly to the pedotransfer
 367 function, mostly on saturation level, as a full saturation means perfect propagation of pressure through the
 368 mixture, and low saturation equates to minimal pressure propagation (Saxton and Rawls., 2006). Additionally it
 369 should depend on pedotransfer functions, and the size distribution of structured solid matrices within the
 370 mixture. For low-saturation levels, it can be assumed no fluid pressure is retained. Combined with an assumed
 371 soil matrix height identical to the total mixture height, this results in $\mathcal{B} = 0$. Assuming saturation of structures
 372 solids results in a full propagation of pressures and $\mathcal{B} = 1$.

373 **ii)Stress-Strain relationship**

374 Depth-averaging the stress-strain relationship in equations 22 and 23 requires a vertical solution for the
 375 internal stress. First, we assume any non-normal vertical terms are zero (Equation 40). Commonly, Rankine
 376 earth pressure coefficients are used to express the lateral earth pressure by assuming vertical stress to be induced
 377 by the basal solid pressure (Equation 41 and 42) (Pitman & Le, 2005; Pudasaini, 2012; Abe & Konagai, 2016).

378 40. $\sigma^{zx} = \sigma^{zy} = \sigma^{yz} = \sigma^{xz} = 0$

379 41. $\bar{\sigma}^{zz} = \frac{1}{2} P_{b_s}, \sigma^{zz}|_b = P_{b_s}$

380 42. $K_a = \frac{1 - \sin(\phi)}{1 + \sin(\phi)}, K_p = \frac{1 + \sin(\phi)}{1 - \sin(\phi)}$

381 Here we enhance this with Bell's extension for cohesive soils (Equation 45) (Richard et al., 2017). This
 382 lateral normal-directed stress term is added to the full stress-strain solution.

383 43. $\bar{\sigma}_{xx} = K\sigma_{zz}|_b - 2c\sqrt{K} + \frac{1}{h} \int_0^h \sigma_{xx} dh$

384 Finally, the gradient in pressure of the lateral interfaces between the mixture is added as a depth-
 385 averaged acceleration term (Equation 44).

386 44. $S_{x_c} = \alpha_c \left(\frac{1}{h} \left(\frac{\partial(h\sigma^{xx})}{\partial x} + \frac{\partial(h\sigma^{yx})}{\partial y} \right) \right) + \dots$

387 **iii)Depth-averaging other terms**

388 While the majority of terms allow for depth-averaging as proposed by Pudasaini (2012), an exception
 389 arises. Depth-averaging of the vertical viscosity terms is required. The non-Newtonian viscous terms for the fluid
 390 phase were derived assuming a vertical profile in the volumetric solid phase content. Here, we alter the
 391 derivation to use this assumption only for the non-structured solids, as opposed to the structured solids where
 392 $\frac{\partial \alpha_s}{\partial z} = 0$.

393 45. $\int_b^s \frac{\partial}{\partial z} \left(\frac{\partial \alpha_s}{\partial z} (u_u - u_c) \right) dz = \left[\frac{\partial \alpha_s}{\partial z} (u_u - u_c) \right]_b^s = (\bar{u}_u - \bar{u}_c) \left[\frac{\partial \alpha_s}{\partial z} \right]_b^s = (\bar{u}_u - \bar{u}_c) \left[\frac{\partial \alpha_s}{\partial z} \right]_b^s =$
 394 $\frac{(\bar{u}_u - \bar{u}_c)(1 - f_{sc})\zeta \alpha_s}{h}$

395 Where ζ is the shape factor for the vertical distribution of solids (Pudasaini, 2012). Additionally, the
396 momentum balance of Pudasaini (2012) ignores any deviatoric stress ($\tau_{xy} = 0$), following Savage and Hutter
397 (2007), and Pudasaini and Hutter (2007). Earlier this term was included by Iverson and Denlinger (2001), Pitman
398 and Le (2005) and Abe & Kanogai (2016). Here we include these terms since a full stress-strain relationship is
399 included.

400 Basal frictions

401 Additionally we add the Darcy-Weisbach friction, which is a Chezy-type friction law for the fluid phase
402 that provides drag (Delestre et al., 2014). This ensures that, without solid phase, a clear fluid does lose
403 momentum due to friction from basal shear. This was successfully done in Bout et al. (2018) and was similarly
404 assumed in Pudasaini and Fischer (2016) for fluid basal shear stress.

$$405 \quad 46. S_f = \frac{g}{n^2} \frac{u_u |u_u|}{h^{\frac{4}{3}}}$$

406 Where n is Manning's surface roughness coefficient.

407 Depth-averaged equations

408 The following set of equations is thus finally achieved for depth-averaged flow over sloping terrain (Equations
409 47-71).

$$410 \quad 47. \frac{\partial h}{\partial t} + \frac{\partial}{\partial x} [h(\alpha_u u_u + \alpha_c u_c)] + \frac{\partial}{\partial y} [h(\alpha_u u_u + \alpha_c u_c)] = R - I$$

$$411 \quad 48. \frac{\partial \alpha_c h}{\partial t} + \frac{\partial \alpha_c h u_c}{\partial x} + \frac{\partial \alpha_c h v_c}{\partial y} = 0$$

$$412 \quad 49. \frac{\partial \alpha_u h}{\partial t} + \frac{\partial \alpha_u h u_u}{\partial x} + \frac{\partial \alpha_u h v_u}{\partial y} = R - I$$

$$413 \quad 50. \frac{\partial}{\partial t} [\alpha_c h (u_c - \gamma_c C_{VM} (u_u - u_c))] + \frac{\partial}{\partial x} [\alpha_c h (u_c^2 - \gamma_c C_{VM} (u_u^2 - u_c^2))] + \frac{\partial}{\partial y} [\alpha_c h (u_c v_c -$$

$$414 \quad \gamma_c C_{VM} (u_u v_u - u_c v_c))] = h S_{x_c}$$

$$415 \quad 51. \frac{\partial}{\partial t} [\alpha_c h (v_c - \gamma_c C_{VM} (v_u - v_c))] + \frac{\partial}{\partial x} [\alpha_c h (u_s v_s - \gamma_c C_{VM} (u_u v_u - u_c v_c))] + \frac{\partial}{\partial y} [\alpha_c h (v_c^2 -$$

$$416 \quad \gamma_c C_{VM} (v_u^2 - v_c^2))] = h S_{y_c}$$

$$417 \quad 52. \frac{\partial}{\partial t} [\alpha_u h (u_u - \frac{\alpha_c}{\alpha_u} C_{VM} (u_u - u_c))] + \frac{\partial}{\partial x} [\alpha_u h (u_u^2 - \frac{\alpha_c}{\alpha_u} C_{VM} (u_u^2 - u_c^2) + \frac{\beta x_u h}{2})] + \frac{\partial}{\partial y} [\alpha_u h (u_u v_u -$$

$$418 \quad \gamma_c C_{VM} (u_u v_u - u_c v_c))] = h S_{x_u} - I u_u$$

$$419 \quad 53. \frac{\partial}{\partial t} [\alpha_u h (v_u - \frac{\alpha_c}{\alpha_u} C_{VM} (v_u - v_c))] + \frac{\partial}{\partial x} [\alpha_u h (u_u v_u - \frac{\alpha_c}{\alpha_u} C_{VM} (u_u v_u - u_c v_c))] + \frac{\partial}{\partial y} [\alpha_u h (v_u^2 -$$

$$420 \quad \gamma_c C_{VM} (v_u^2 - v_c^2) + \frac{\beta y_u h}{2})] = h S_{y_u} - I v_u$$

$$421 \quad 54. S_{x_c} = \alpha_c \left[g^x + \frac{1}{h} \left(\frac{\partial (h \sigma^{xx})}{\partial x} + \frac{\partial (h \sigma^{xy})}{\partial y} \right) - P_{bc} \left(\frac{u_c}{|u_c|} \tan \phi + \epsilon \frac{\partial b}{\partial x} \right) \right] - \epsilon \alpha_c \gamma_c p_{bu} \left[\frac{\partial h}{\partial x} + \frac{\partial b}{\partial x} \right] +$$

$$422 \quad C_{DG} (u_u - u_c) |u_u - u_c|^{J-1}$$

$$423 \quad 55. S_{y_c} = \alpha_c \left[g^y + \frac{1}{h} \left(\frac{\partial (h \sigma^{xy})}{\partial x} + \frac{\partial (h \sigma^{yy})}{\partial y} \right) - P_{bc} \left(\frac{v_s}{|u_s|} \tan \phi + \epsilon \frac{\partial b}{\partial y} \right) \right] - \epsilon \alpha_c \gamma_c p_{bu} \left[\frac{\partial h}{\partial y} + \frac{\partial b}{\partial y} \right] +$$

$$424 \quad C_{DG} (v_u - v_c) |v_u - v_c|^{J-1}$$

$$425 \quad 56. S_{x_u} = \alpha_u \left[g^x - \frac{1}{2} \frac{p_{bu} h}{\alpha_u} \frac{\partial \alpha_c}{\partial x} + P_{bu} \frac{\partial b}{\partial x} - \frac{\mathcal{A} \eta_u}{\alpha_u} \left(2 \frac{\partial^2 u_u}{\partial x^2} + \frac{\partial^2 v_u}{\partial x y} + \frac{\partial^2 u_u}{\partial y^2} - \frac{X u_u}{\epsilon^2 h^2} \right) + \frac{\mathcal{A} \eta_u}{\alpha_u} \left(2 \frac{\partial}{\partial x} \left(\frac{\partial}{\partial x} (u_u - u_c) \right) + \right.$$

$$426 \quad \left. \frac{\partial}{\partial y} \left(\frac{\partial \alpha_c}{\partial x} (v_u - v_c) + \frac{\partial \alpha_u}{\partial y} (u_u - u_c) \right) \right) - \frac{\mathcal{A} \eta_u \zeta \alpha_s (1 - f_{sc}) (u_u - u_c)}{\alpha_u h^2} - \frac{g}{n^2} \frac{u_u |u_u|}{h^{\frac{4}{3}}} \right] - \frac{1}{\gamma_c} C_{DG} (u_u -$$

$$427 \quad u_c) |u_u - u_c|^{J-1}$$

$$428 \quad 57. S_{y_u} = \alpha_u \left[g^y - \frac{1}{2} \frac{p_{bu} h}{\alpha_u} \frac{\partial \alpha_c}{\partial y} + P_{bu} \frac{\partial b}{\partial y} - \frac{\mathcal{A} \eta_u}{\alpha_u} \left(2 \frac{\partial^2 u_f}{\partial y^2} + \frac{\partial^2 v_f}{\partial x y} + \frac{\partial^2 u_f}{\partial x^2} - \frac{X u_f}{\epsilon^2 h^2} \right) + \frac{\mathcal{A} \eta_u}{\alpha_u} \left(2 \frac{\partial}{\partial y} \left(\frac{\partial}{\partial y} (v_u - \right.$$

$$429 \quad v_c) \right) + \frac{\partial}{\partial x} \left(\frac{\partial \alpha_c}{\partial y} (u_u - u_c) + \frac{\partial \alpha_u}{\partial x} (v_u - v_c) \right) \right) - \frac{\mathcal{A} \eta_u \zeta \alpha_s (1 - f_{sc}) (v_u - v_c)}{\alpha_u h^2} - \frac{g}{n^2} \frac{v_u |u_u|}{h^{\frac{4}{3}}} \right] - \frac{1}{\gamma_c} C_{DG} (v_u -$$

$$430 \quad v_c) |u_u - u_c|^{J-1}$$

$$431 \quad 58. P_{bc} = -(1 - f_{sc})(1 - \gamma) \frac{(1 - f_{sc}) \alpha_s}{(1 - f_{fc}) \alpha_f} g^z h - f_{sc} (1 - \gamma) \frac{(f_{sc}) \alpha_s}{(f_{fc}) \alpha_f} g^z h$$

435
436
437
438
439
440
441
442
443
444
445
446
447
448
449

$$\begin{aligned}
59. P_{bu} &= -g^z h \\
60. \gamma_c &= \frac{\rho_u}{\rho_c}, \gamma = \frac{\rho_f}{\rho_s} \\
61. C_{DG} &= \frac{f_{sc}\alpha_c\alpha_u(\rho_c-\rho_f)g}{U_{T,c}(g(Re)) + S_p} + \frac{(1-f_{sc})\alpha_c\alpha_u(\rho_s-\rho_f)g}{U_{T,uc}(\mathcal{P}\mathcal{F}(Re_p) + (1-\mathcal{P})g(Re)) + S_p} \\
62. S_p &= \left(\frac{\mathcal{P}}{\alpha_c} + \frac{1-\mathcal{P}}{\alpha_u}\right)\mathcal{K} \\
63. \mathcal{K} &= |\alpha_c \mathbf{u}_c + \alpha_u \mathbf{u}_u| \\
64. F &= \frac{\gamma}{180} \left(\frac{\alpha_f}{\alpha_s}\right)^3 Re_p, G = \alpha_f^{M(Re_p)-1}, Re_p = \frac{\rho_f d U_t}{\eta_f}, N_R = \frac{\sqrt{gLH\rho_f}}{\alpha_f \eta_f}, N_{RA} = \frac{\sqrt{gLH\rho_f}}{A\eta_f} \\
65. C_{Vm} &= \left(\frac{1}{2} \left(\frac{1+2\alpha_c}{\alpha_u}\right)\right) \\
66. \dot{\delta} &= \sigma^{\alpha\gamma} \dot{\omega}^{\beta\gamma} + \sigma^{\gamma\beta} \dot{\omega}^{\alpha\gamma} + 2G \dot{\epsilon}^{\alpha\beta} + K \dot{\epsilon}^{\gamma\gamma} \delta^{\alpha\beta} - \dot{\lambda} \left[9K \sin\psi \delta^{\alpha\beta} + \frac{G}{\sqrt{J_2}} s^{\alpha\beta} \right] \\
67. \dot{\lambda} &= \frac{3\alpha K \dot{\epsilon}^{\gamma\gamma} + \left(\frac{G}{\sqrt{J_2}}\right) s^{\alpha\beta} \dot{\epsilon}^{\alpha\beta}}{27\alpha_\phi K \sin\psi + G} \\
68. K &= \frac{E}{3(1-2\nu)}, G = \frac{E}{2(1+\nu)} \\
69. \sigma^{\alpha\beta} &= s^{\alpha\beta} + \frac{1}{3} \sigma^{\gamma\gamma} \delta^{\alpha\beta} \\
70. \dot{\epsilon}^{\alpha\beta} &= \frac{1}{2} \left(\frac{\partial v^\alpha}{\partial x^\beta} - \frac{\partial v^\beta}{\partial x^\alpha} \right) \quad \dot{\omega}^{\alpha\beta} = \frac{1}{2} \left(\frac{\partial v^\alpha}{\partial x^\beta} + \frac{\partial v^\beta}{\partial x^\alpha} \right) \\
71. \alpha_\phi &= \frac{\tan(\phi)}{\sqrt{9+12 \tan^2 \phi}} \quad k_c = \frac{3c}{\sqrt{9+12 \tan^2 \phi}}
\end{aligned}$$

450 Where X is the shape factor for vertical shearing of the fluid ($X \approx 3$ in Iverson & Denlinger, 2001), R is the
451 precipitation rate and I is the infiltration rate.

452
453 **Closing the equations**

454 Viscosity is estimated using the empirical expression from O'Brien and Julien (1985), which relates dynamic
455 viscosity to the solid concentration of the fluid (Equation 72).

456 72. $\eta = \alpha e^{\beta\alpha_s}$

457 Where α is the first viscosity parameter and β the second viscosity parameter.

458 Finally, the settling velocity of small ($d < 100 \mu m$) grains is estimated by Stokes equations for a
459 homogeneous sphere in water. For larger grains ($> 1mm$), the equation by Zanke (1977) is used (Equation 30).

460 73.
$$U_T = 10 \frac{\eta}{d} \left(\sqrt{1 + \frac{0.01 \left(\frac{\rho_s - \rho_f}{\rho_f} \right) g d^3}{\eta}} - 1 \right)$$

461 In which U_T is the settling (or terminal) velocity of a solid grain, η is the dynamic viscosity of the fluid,
462 ρ_f is the density of the fluid, ρ_s is the density of the solids, d is the grain diameter (m)

463
464 **2.4 Implementation in the Material Point Method numerical scheme**

465 Implementing the presented set of equations into a numerical scheme requires considerations of that
466 schemes limitations and strengths (Stomakhin et al., 2013). Fluid dynamics are almost exclusively solved using
467 an Eulerian finite element solution (Delestre et al., 2014; Bout et al., 2018). The diffusive advection part of such
468 scheme typically doesn't degrade the quality of modelling results. Solid material however is commonly
469 simulated with higher accuracy using an Lagrangian finite element method or discrete element method (Maurel
470 & Cumbescure, 2008; Stomakhin et al., 2013). Such schemes more easily allow for the material to maintain its
471 physical properties during movement. Additionally, advection in these schemes does not artificially diffuse the
472 material since the material itself is discretized, instead of the space (grid) on which the equations are solved. In
473 our case, the material point method (MPM) provides an appropriate tool to implement the set of presented
474 equations (Bui et al., 2008; Maurel & Cumbescure, 2008; Stomakhin et al., 2013). Numerous existing modelling
475 studies have implemented in this method (Pastor et al., 2007; Pastor et al., 2008; Abe & Kanogai, 2016). Here,
476 we use the MPM method to create a two-phase scheme. This allows the usage of finite elements aspects for the

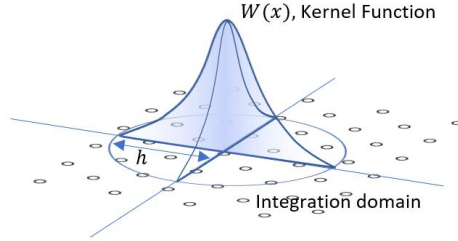
477 fluid dynamics, which are so successfully described by the that method (particularly for water in larger areas, see
478 Bout et al., 2018).

479 Mathematical Framework

480 The mathematic framework of smooth-particles solves differential equations using discretized volumes
481 of mass represented by kernel functions (Lidersky & Petschek, 1991; Bui et al., 2008; Stomakhin et al., 2013).
482 Here, we use the cubic spline kernel as used by Monaghan (2000) (Equation 74).

$$483 \quad 74. \quad W(r, h) = \begin{cases} \frac{10}{7\pi h^2} \left(1 - \frac{3}{2}q^2 + \frac{3}{4}q^3\right) & 0 \leq |q| \leq 2 \\ \frac{10}{28\pi h^2} (2 - q)^3 & 1 \leq |q| < 2 \\ 0 & |q| \geq 2 \mid q < 0 \end{cases}$$

484 Where r is the distance, h is the kernel size and q is the normalized distance ($q = \frac{r}{h}$)



485
486 *Figure 2 Example of a kernel function used as integration domain for mathematical operations.*

487 Using this function mathematical operators can be defined. The average is calculated using a weighted
488 sum of particle values (Equation 75) while the derivative depends on the function values and the derivative of
489 the kernel by means of the chain rule (Equation 76) (Lidersky & Petschek, 1991; Bui et al., 2008).

$$490 \quad 75. \quad \langle f(x) \rangle = \sum_{j=1}^N \frac{m_j}{\rho_j} f(x_j) W(x - x_j, h)$$

$$491 \quad 76. \quad \left\langle \frac{\partial f(x)}{\partial x} \right\rangle = \sum_{j=1}^N \frac{m_j}{\rho_j} f(x_j) \frac{\partial W_{ij}}{\partial x_i}$$

492 Where $W_{ij} = W(x_i - x_j, h)$ is the weight of particle j to particle i , $r = |x_i - x_j|$ is the distance
493 between two particles. The derivative of the weight function is defined by equation 77.

$$494 \quad 77. \quad \frac{\partial W_{ij}}{\partial x_i} = \frac{x_i - x_j}{r} \frac{\partial W_{ij}}{\partial r}$$

495 Using these tools, the momentum equations for the particles can be defined (Equations 78-84). Here, we
496 follow Monaghan (1999) and Bui et al. (2008) for the definition of artificial numerical forces related to stability.
497 Additionally, stress-based forces are calculated on the particle level, while other momentum source terms are
498 solved on a Eulerian grid with spacing h (identical to the kernel size).

$$499 \quad 78. \quad \frac{dv_i^\alpha}{dt} = \frac{1}{m_i} (F_g + F_{grid}) + \sum_{j=1}^N m_j \left(\frac{\sigma_i^{\alpha\beta}}{\rho_i^2} + \frac{\sigma_j^{\alpha\beta}}{\rho_j^2} + F_{ij}^n R_{ij}^{\alpha\beta} + \Pi_{ij} \delta^{\alpha\beta} \right) \frac{\partial W_{ij}}{\partial x_i^\beta}$$

$$500 \quad 79. \quad \epsilon^{\alpha\beta} = \frac{1}{2} \left(\sum_{j=1}^N \frac{m_j}{\rho_j} (v_j^\alpha - v_i^\alpha) \frac{\partial W_{ij}}{\partial x_i^\beta} + \sum_{j=1}^N \frac{m_j}{\rho_j} (v_j^\beta - v_i^\beta) \frac{\partial W_{ij}}{\partial x_i^\alpha} \right)$$

$$501 \quad 80. \quad \omega^{\alpha\beta} = \frac{1}{2} \left(\sum_{j=1}^N \frac{m_j}{\rho_j} (v_j^\alpha - v_i^\alpha) \frac{\partial W_{ij}}{\partial x_i^\beta} - \sum_{j=1}^N \frac{m_j}{\rho_j} (v_j^\beta - v_i^\beta) \frac{\partial W_{ij}}{\partial x_i^\alpha} \right)$$

$$502 \quad 81. \quad \frac{d\sigma_{\alpha\beta}}{dt} = \sigma_i^{\alpha\gamma} \omega_i^{\beta\gamma} + \sigma_i^{\gamma\beta} \omega_i^{\alpha\gamma} + 2G_i \epsilon_i^{\alpha\beta} + K_i \epsilon^{\gamma\gamma} \delta_i^{\alpha\beta} - \lambda_i \left[9K_i \sin\psi_i \delta^{\alpha\beta} + \frac{G_i}{\sqrt{J_{2i}}} s_i^{\alpha\beta} \right]$$

$$503 \quad 82. \quad \lambda_i = \frac{3\alpha K_i \epsilon_i^{\gamma\gamma} + \left(\frac{G_i}{\sqrt{J_{2i}}} \right) s_i^{\alpha\beta} \epsilon_i^{\alpha\beta}}{27\alpha_\phi K_i \sin\psi_i + G_i}$$

504 Where i, j are indices indicating the particle, Π_{ij} is an artificial viscous force as defined by equations 83
505 and 84 and $F_{ij}^n R_{ij}^{\alpha\beta}$ is an artificial stress term as defined by equations 85 and 86.

$$\begin{aligned}
506 \quad 83. \quad \Pi_{ij} &= \begin{cases} \frac{\alpha_{\Pi} u_{\text{sound}} \phi_{ij} + \beta_{\Pi} \phi^2}{\rho_{ij}} & v_{ij} \cdot x_{ij} < 0 \\ 0 & v_{ij} \cdot x_{ij} \geq 0 \end{cases} \\
507 \quad 84. \quad \phi_{ij} &= \frac{h_{ij} v_{ij} x_{ij}}{|x_{ij}|^2 + 0.01 h_{ij}^2}, \quad x_{ij} = x_i - x_j, \quad v_{ij} = v_i - v_j, \quad h_{ij} = \frac{1}{2}(h_i + h_j) \\
508 \quad 85. \quad F_{ij}^n R_{ij}^{\alpha\beta} &= \left[\frac{W_{ij}}{W(d_0, h)} \right]^n (R_i^{\alpha\beta} + R_j^{\alpha\beta}) \\
509 \quad 86. \quad \overline{R_i^{\gamma\gamma}} &= -\frac{\epsilon_0 \sigma_i^{\gamma\gamma}}{\rho_i^2}
\end{aligned}$$

510 Where ϵ_0 is a small parameter ranging from 0 to 1, α_{Π} and β_{Π} are constants in the artificial viscous
511 force (often chosen close to 1), u_{sound} is the speed of sound in the material.

512 The conversion from particles to gridded values and reversed depends on a grid basis function that
513 weighs the influence of particle values for a grid center. Here, a function derived from dyadic products of one-
514 dimensional cubic B-splines is used as was done by Steffen et al. (2008) and Stomakhin et al. (2013) (Equation
515 84).

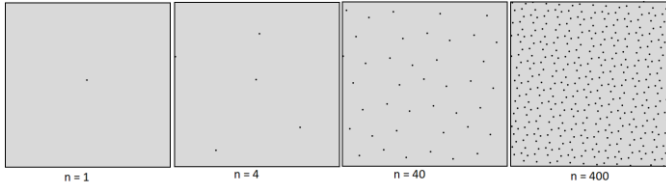
$$516 \quad 87. \quad N(x) = N(x^x) * N(x^y), \quad N(x) = \begin{cases} \frac{1}{2}|x|^3 - x^2 + \frac{2}{3} & 0 \leq |x| \leq 2 \\ -\frac{1}{6}|x|^3 + x^2 - 2|x| + \frac{4}{3} & 1 \leq |x| < 2 \\ 0 & |x| \geq 2 \end{cases}$$

517 Particle placement

518 Particle placement is typically done in a constant pattern, as initial conditions have some constant
519 density. The simplest approach is a regular square or triangular network, with particles on the corners of the
520 network. Here, we use an approach that is more adaptable to spatially-varying initial flow height. The R_2
521 sequence approaches, with a regular quasirandom sequence, a set of evenly distributed points within a square
522 (Roberts, 2020) (Equation 85).

$$523 \quad 88. \quad x_n = n\alpha \bmod 1, \quad \alpha = \left(\frac{1}{c_p}, \frac{1}{c_p} \right)$$

524 Where x_n is the relative location of the n^{th} particle within a gridcell, $c_p = \left(\frac{9+\sqrt{69}}{18} \right)^{\frac{1}{3}} + \left(\frac{9-\sqrt{69}}{18} \right)^{\frac{1}{3}} \approx$
525 1.32471795572 is the plastic constant.



526
527 *Figure 3 Example particle distributions using the R_2 sequence, note that, while not all particles are*
528 *equidistant, the method produces distributed particle patterns that adapt well to varying density.*

529 The number of particles placed for a particular flow height depends on the particle volume V_l , which is
530 taken as a global constant during the simulation.

531 3. Flume Experiments

532 3.03.1 Flume Setup

533 In order to validate the presented model, several controlled experiments were performed and reproduced
534 using the developed equations. The flume setup consists of a steep incline, followed by a near-flat runout plane
535 (Figure 3). A massive obstacle is placed on the separation point of the two planes. This blocks the path of two
536 fifths of the width of the moving material. For the exact dimensions of both the flume parts and the obstacle, see
537 figure 3.

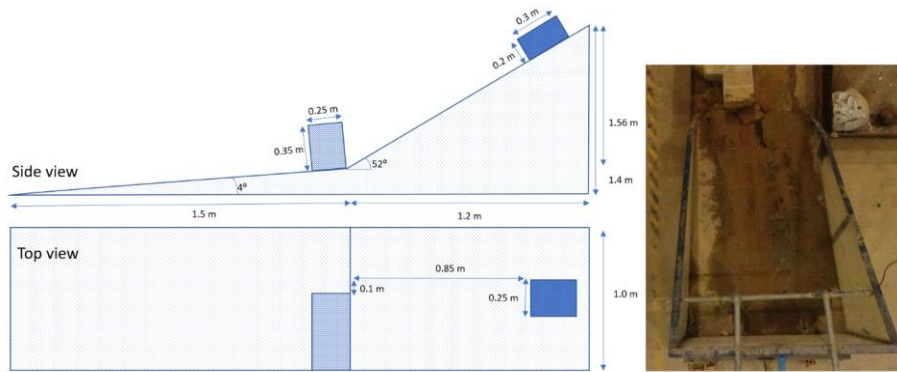


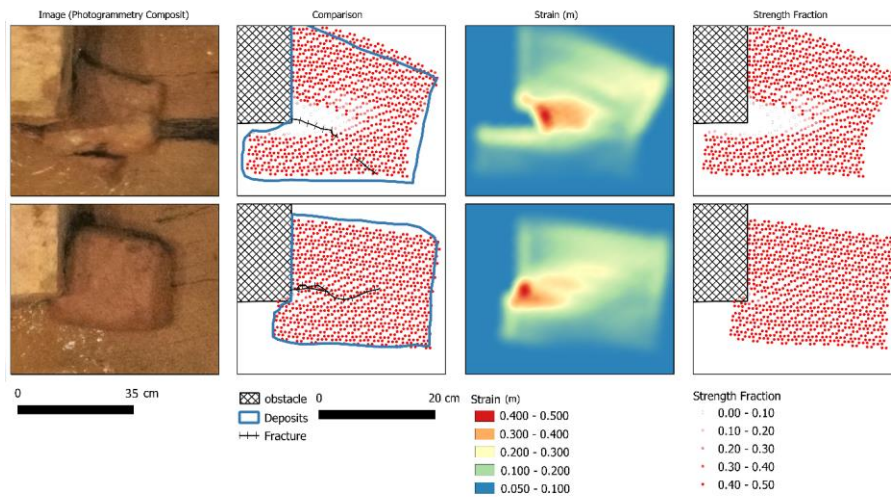
Figure 4 The dimensions of the flume experiment setup used in this work.

538
539

540 Two tests were performed whereby a cohesive granular matrix was released at the upper part of the
 541 flume setup. Both of these volumes had dimensions of 0.2x0.3x0.25 meter (height,length,width). For both of
 542 these materials, a mixture high-organic content silty-clay soils were used. The materials strength parameters
 543 were obtained using tri-axial testing (Cohesion, internal friction angle Youngs modulus and Poisson Ration. The
 544 first set of materials properties where $c = 26.7$ kPa and $\phi = 28^\circ$. The second set materials properties where $c =$
 545 18.3 kPa and $\phi = 27^\circ$. For both of the events, pre-and post release elevations models were made using
 546 photogrammetry. The model was set up to replicate the situations using the measured input parameters.
 547 Numerical settings were chosen as $\{\alpha_s = 0.5, \alpha_f = 0.5, f_{sc} = 1.0, f_{fc} = 1.0, \rho_f = 1000, \rho_s = 2400, E = 12 \cdot$
 548 $10^6 Pa, K = 23 \cdot 10^6 Pa, \psi = 0, \alpha_{\Pi} = 1, \beta_{\Pi} = 1, X, \zeta, j = 2, u_{sound} = 600, dx = 10, V_l = , h = 10, n =$
 549 $0.1, \alpha = 1, \beta = 10, M = 2.4, B = 0, N_R = 15000, N_{RA} = 30\}$. Calibration was performed by means of input
 550 variation. The solid fraction, and elastic and bulk modulus were varied between 20 and 200 percent of their
 551 original values with increments of 10 percent. Accuracy was assessed based on the percentage accuracy of the
 552 deposition (comparison of modelled vs observed presence of material).

553 3.03.2 Results

554 Both the mapped extent of the material after flume experiments, as the simulation results are shown in
 555 figure 5. Calibrated values for the simulations are $\{\alpha_s = 0.45, E = 21.6 \cdot 10^6 Pa, K = 13.8 \cdot 10^6 Pa\}$.



556
 557 *Figure 5 A comparison of the final deposits of the simulations and the mapped final deposits and cracks*
 558 *within the material. From left to right: Photogrammetry mosaic, comparison of simulation results to mapped*
 559 *flume experiment, strain, final strength fraction remaining.*

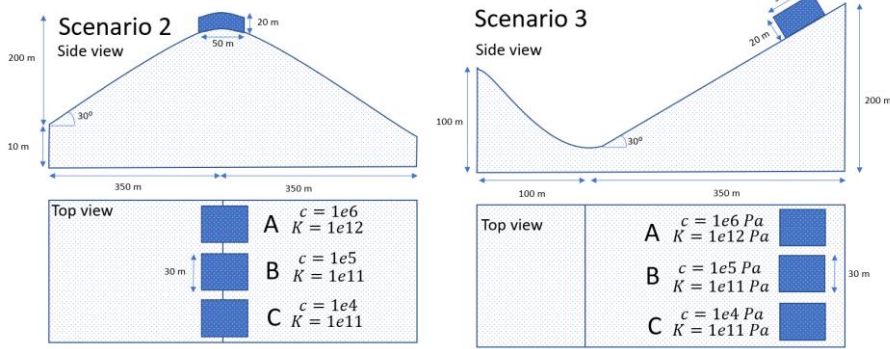
560 As soon as the block of material impacts the obstacle, stress increases as the moving objects is
 561 deformed. This stress quickly propagates through the object. Within the scenario with lower cohesive strength,
 562 as soon as the stress reached beyond the yield strength, degradation of strength parameters took place. In the
 563 results, a fracture line developed along the corner of the obstacle into the length direction of the moving mass.
 564 Eventually, this fracture developed to half the length of the moving body and severe deformation resulted. As
 565 was observed from the tests, the first material experienced a critical fracture while the second test resulted in
 566 moderate deformation near the impact location. Generally, the results compare well with the observed patters,
 567 although the exact shape of the fracture is not replicated. Several reasons might be the cause of the moderately
 568 accurate fracture patterns. Other studies used a more controlled setup where uncertainties in applied stress and
 569 material properties were reduced. Furthermore, the homogeneity of the material used in the tests can not
 570 completely assumed. Realistically, minor alterations in compression used to create the clay blocks has left spatial
 571 variation in density, cohesion and other strength parameters.

572 4. Numerical Tests

573 4.1 Numerical Setup

574 In order to further investigate some of the behaviors of the model, and highlight the novel types of mass
 575 movement dynamics that the model implements, several numerical tests have been performed. The setup of these
 576 tests is shown in figure 6.

577



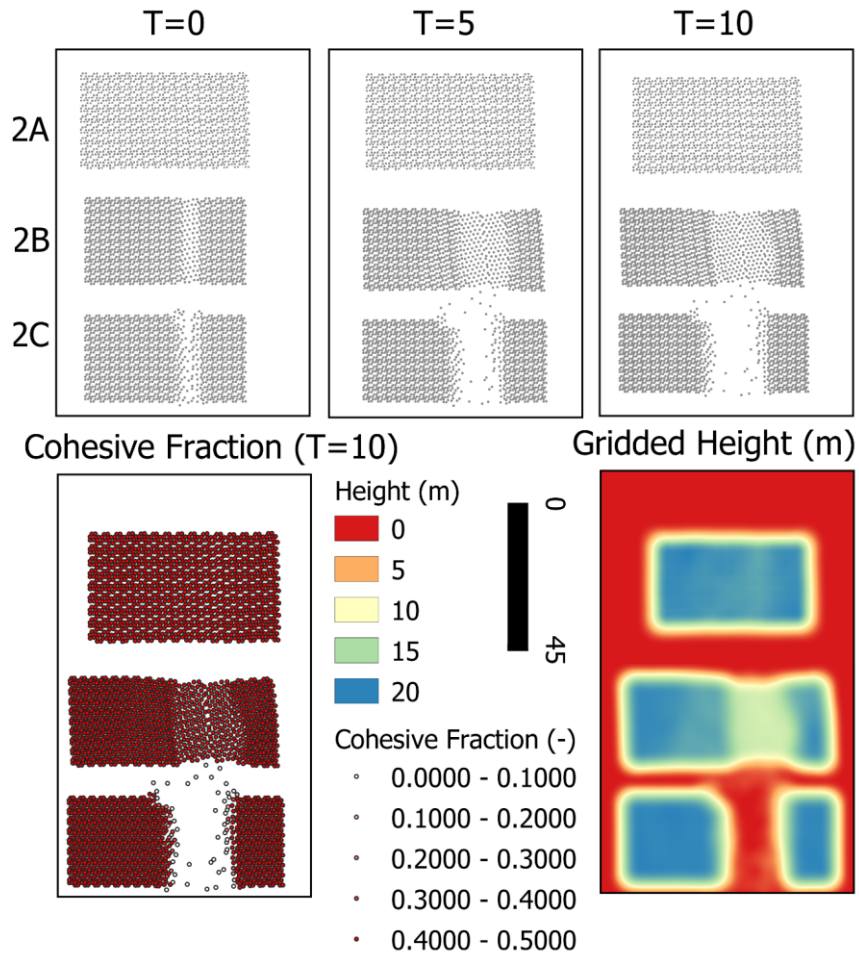
578
579 *Figure 6 The dimensions of the numerical experiment setups used in this work. Setup 1 (left) and Setup 2 (right)*

580 Numerical settings were chosen for three different blocks with equal volume but distinct properties.
581 Cohesive strength and the bulk modulus were varied (see figure 6). Remaining parameters were chosen as
582 $\{\alpha_s = 0.5, \alpha_f = 0.5, f_{sc} = 1.0, f_{fc} = 1.0, \rho_f = 1000 \text{ kgm}^{-3}, \rho_s = 2400 \text{ kgm}^{-3}, E = 1e12 \text{ Pa}, \psi = 0, \alpha_{\Pi} =$
583 $1, \beta_{\Pi} = 1, X, \zeta, j = 2, u_{sound} = 600 \text{ ms}^{-1}, dx = 10 \text{ m}, V_l, h = 10 \text{ m}, n = 0.1, \alpha = 1, \beta = 10, M = 2.4, \mathcal{B} =$
584 $0, N_R = 15000, N_{RA} = 30\}$.

585 **4.2 Results**

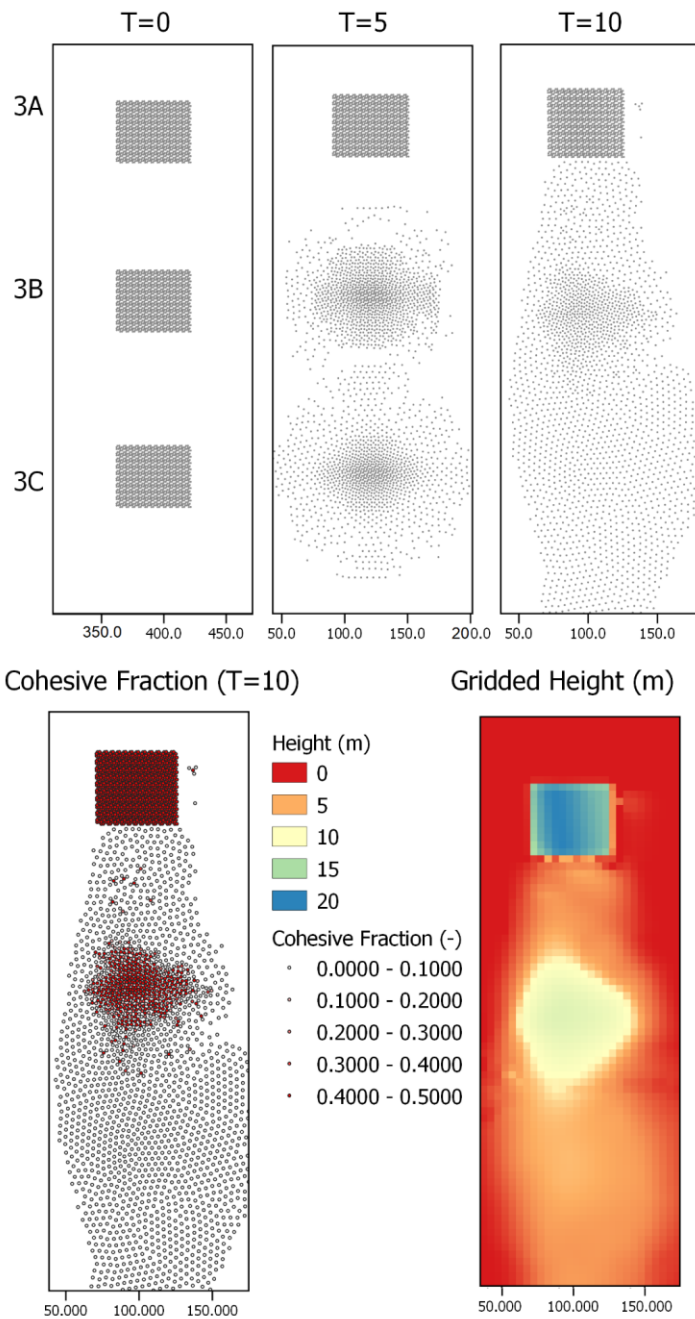
586 Several time-slices for the described numerical scenarios are shown in figure 7 and 8.

587



588

589 *Figure 7 Several time-slices for numerical scenarios 2(A/B/C). See figure 6 for the dimensions and*
 590 *terrain setup.*



591
592 *Figure 8 Several time-slices for numerical scenarios 3(A/B/C). See figure 6 for the dimensions and terrain setup.*

593 Fractures develop in the mass movements based on acceleration differences and cohesive strength. For
594 scenario 2A, the stress state does not reach beyond the yield surface, and all material is moved as a single block.
595 Scenario 2B, which features lowered cohesive strength, fractures and the masses separate based on the
596 acceleration caused by slopes.

597 Fracturing behavior can occur in MPM schemes due to numerical limitations inherent in the usage of a
598 limited integration domain. Here, validation of real physically-based fracturing is present in the remaining
599 cohesive fraction. This value only reduces in case of plastic yield, where increasing strain degrades strength
600 parameters according to our proposed criteria. Numerical fractures would thus have a cohesive fraction of 1. In
601 all simulated scenarios, such numerical issues were not observed.

602 Fragmentation occurs due to spatial variation in acceleration in the case of scenario 3A and 3B. For
603 scenario 3A, the yield surface is not reached and the original structure of the mass is maintained during
604 movement. For 3C, fragmentation is induced by lateral pressure and buoyancy forces alone. Scenario 3B
605 experiences slight fragmentation at the edges of the mass, but predominantly fragments when reaching the
606 valley, after which part of the material is accelerated to count to the velocity of the mass. For all the shown
607 simulations, fragmentation does not lead to significant phase separation since virtual mass and drag forces
608 converge the separate phase velocities to their mixture-averaged velocity. The strength of these forces partly
609 depends on the parameters, effects of more immediate phase-separation could be studied if other parameters are
610 used as input.

611 5. Discussion

612 A variety of existing landslide models simulate the behavior of lateral connected material through a
613 non-linear, non-Newtonian viscous relationship (Boetticher et al., 2016; Fornes et al., 2017; Pudasaini &
614 Mergili, 2019; Greco et al., 2019). These relationships include a yield stress and are usually regularized to
615 prevent singularities from occurring. While this approach is incredibly powerful, it is fundamentally different
616 from the work proposed here. These viscous approaches do not distinguish between elastic or plastic
617 deformation, and typically ignore deformations if stress is insufficient. Additionally, fracturing is not
618 implemented in these models. The approach taken in this work attempts to simulate a full stress-strain
619 relationship with Mohr-Coulomb type yield surface. This does provide new types of behavior and can be
620 combined with non-Newtonian viscous approaches as mentioned above. A major downside to the presented
621 work is the steep increase in computational time required to maintain an accurate and stable simulation.
622 Commonly, an increase of near a 100 times has been observed during the development of the presented model.

623 The presented model shows a good likeness to flume experiments and numerical tests highlight
624 behavior that is commonly observed for landslide movements. There are however, inherent scaling issues and the
625 material used in the flume experiments is unlikely to form larger landslide masses. The measured physical
626 strength parameters of the material used in the flume experiments would not allow for sustained structured
627 movement at larger scales. There is thus the need for more, real-scale, validation cases. The application of the
628 presented type of model is most directly noticeable for block-type landslide movements that have fragmented
629 either upon impact of some obstacle or during transition phase. Of importance here is that the moment of
630 fragmentation is often not reported in studies on fast-moving landslides, potentially due to the complexities in
631 knowing the details on this behavior from post-event evidence. Validation would therefore have to occur on
632 cases where deposits are not fully fragmented, indicating that this process was ongoing during the whole
633 movement duration. The spatial extent of initiation and deposition would then allow validation of the model.
634 Another major opportunity for validation of the novel aspects of the model is the full three-dimensional
635 application to landslides that were reported to have lubrication effects due to fragmentation of lower fraction of
636 flow due to shear.

637 An important point of consideration in the development of complex multi-process generalized models is
638 the applicability. As a detailed investigative research tool, these models provide a basic scenario of usage.
639 However, both for research and beyond this, in applicability in disaster risk reduction decision support, the
640 benefit drawn from these models depends on the practical requirement for parameterization and the
641 computational demands for simulation. With an increasing complexity in the description of multi-process
642 mechanics comes the requirement of more measured or estimated physical parameters. Inspection of the
643 presented method shows that in principle, a minor amount of new parameters are introduced. The cohesive
644 strength, a major focus of the model, becomes highly important depending on the type of movement being
645 investigated. Additionally, the bulk and elastic modulus are required. These three parameters are common
646 simulation parameters in geotechnical research and can be obtained from common tests on sampled material
647 (Alsalmán et al., 2015). Finally, the basal pressure propagation parameter (\mathcal{B}) is introduced. However, within
648 this work, the value of this parameter is chosen to have a constant value of one. As a result, the model does
649 require additional parameters, although these are relatively easy to obtain with accuracy.

650 There are a variety of aspects of the model that could be significantly improved. Here, we list several
651 major opportunities of future research.

652 **1) Groundwater mechanics**

653 The presented model allows for the a solid or granular matrix to be present within the flow. We have
654 assumed the flows in and out of these matrices are sufficiently small to be ignored. In reality, there is a
655 fluid flux in and out of structured solids. This could occur both due to pressure differences as due to
656 stress and strain of the structured solids. Implementing this kind of mechanics requires a dynamic,
657 solid-properties dependent, soil water retention curve (Van Looy et al., 2017). An example of MPM soil
658 mechanics with dynamic groundwater implementation can be found in Bandera et al. (2016).

659 **2) Implementing Entrainment and Deposition**

660 Current equations for entrainment (erosion with major grain-grain interactions) is limited to
661 unstructured mixture flows (Iverson, 2012; Iverson & Ouyang, 2015; Cuomo et al., 2016; Pudasaini &
662 Fischer, 2016). Extending these models to include a contribution from structured solids would be
663 required to implement entrainment in the presented work.

664 **3) Separation of phases**

665 A major assumption in the presented work is that the velocities of structured solids, free solids and
666 confined fluids are all equal. In reality, there might be separation of structured and free solids phases.
667 Additionally, we already discussed the possibility of in-and outflux of confined fluids from the solid
668 matrix. Recent innovations on three-phase mixture flows might be used to extend the presented work to
669 a three, four or five-phase model by separating free solids, confined fluids or adding a Bingham-viscous
670 solid-fluid phase (Pudasaini & Mergili, 2019). However, while this would implement an additional
671 process, it would significantly increase complexity of the equations (in an exponential manner with
672 relation to the number of phases) and the numerical solutions which could hinder practical applicability.

673 **4) Application to large, slow moving landslides.**

674 When confined fluids would act as a distinct phase, guided by the mechanics of water flow in granular
675 matrix, ground water pressures and movement through the structured solids could be described. This
676 might enable the model to do detailed deformation/groundwater simulation of large slow-moving
677 landslides.

678 **5) Numerical Improvements**

679 Numerical techniques for particle-based discretized methods (SPH, MPM) have been proposed in the
680 literature. A common issue is numerical fracturing of materials when particle strain increases beyond
681 the length of the kernel function. Then, the connection between particles is lost and fracturing occurs as
682 an artifact of the numerical method. This issue is partly solved by the artificial stress term as is also
683 used by Bui et al. (2008). Additionally, geometric subdivide, as used by Xu et al. (2012) and Li et al.
684 (2015), could counter these artificial fractures. Implementing this technique does require additional
685 work to maintain mass and momentum conservation.

686 **6) Three-dimensional solutions**

687 In a variety of scenarios, the assumptions made in depth-averaged application of flow models are
688 invalid. A common example is the impact of mass movements into lakes, or other large water bodies. In
689 such cases, the vertical velocity and concentration variables are not well-described by their depth-
690 averaged counterparts. Additionally, the lubrication effect of basal fragmentation of landslides due to
691 shear can not be described without velocity-profiles and a vertical stress-solution. Full three-
692 dimensional application would therefore have the potential to increase understanding on these important
693 processes.

694 **5. Conclusions**

695 We have presented a novel generalized mass movement model that can describe both unstructured
696 mixture flows and Structured movements of Mohr-Coulomb type material. The presented equations are part of
697 the continuous development of the OpenLISEM Hazard model, an open-source tool for physically-based multi-
698 hazard simulations. The model builds on the works of Pudasaini (2012) and Bui et al. (2008) to develop a single
699 holistic set of equations. The model was implemented in a GPU-based Material Point Method (MPM) Code. The
700 equations were validated on flume experiments and numerical tests, that highlight the new movement dynamics
701 possible with the presented model. The integration of cohesive structure and a full stress-strain relationship for
702 the structured solids allows for movement of block-type slides as a single whole. Interactions with terrain, other
703 flow masses or obstacles lead to elastic-plastic deformation and eventually fragmentation. This type of self-
704 alteration of flow properties is novel with mass movement models. Although the presented equations can provide
705 additional detail for specific mass movement types, applicability of the model for real events need to be
706 investigated as computational costs are significantly increased.

707 The presented simulation both validate the basic behavior of the model, as well as highlight the types of
708 flow dynamics made possible by the presented equations. The models dependency of breaking to cohesive
709 strength and internal friction angle matches the flume experiments. The numerical examples show commonly-
710 described behavior for landslide movements. Although the simulations compare well to the flume experiments,
711 validation is required for real-scale application to various types of mass movements. Additionally, the presented
712 equations still lack descriptions of processes that might become important. Separating the fluid and solid phases
713 such as done by Pudasaini & Mergili (2019), could improve flow dynamics and phase separation. With added
714 ground-water mechanics, such as done in Bandera et al. (2016), slow-moving landslide simulations might be
715 described.

716 **6. Code and Data Availability**

717 All code and data used within this work are made open-source as part of the continuous development of
718 the OpenLISEM Hazard model under the GNU General Public Licence v3.0. The code and the data are hosted
719 on Github (<https://github.com/bastianvandenbout/OpenLISEM-Hazard-2.0-Pre-Release>). Both binaries
720 and a copy of the source code are also available on Sourceforge, where the manual and compilation guide can
721 similarly be found (<https://sourceforge.net/projects/lisem/>). Finally, more information can be found at the blog
722 (<https://blog.utwente.nl/lisem/>)

723 The software, and its user interface, are written for windows, but platform independent libraries are
724 used and compilation might be performed on other platforms.
725 Hardware requirements for the usage of the model are a 64-bit Operating system that can compile all required
726 external libraries (see the manual for a full list and description). A graphical processing unit conforming to at
727 least the OpenCL 1.2 standard and support for both OpenGL 4.2 and OpenGL/OpenCL interoperability.
728 Additionally, an approximate 500 mb of hard drive space and 750 mb of memory must be available.

729

730 **Appendix A. List of Symbols**

- 731 h is the flow height
732 s is the solid phase
733 f is the fluid phase
734 sc is the structured solid phase
735 fc is the confined fluid phase
736 ρ_f is the density of fluids
737 ρ_s is the density of solids
738 α_f is the volumetric fluid phase fraction
739 α_s is the volumetric solid phase fraction
740 f_{sc} is the fraction of solids that is structured (confining)
741 f_{fc} is the fraction of fluids that is confined
742 α_c is the volumetric fraction of solids, structured solids and confined fluids
743 α_u is the volumetric fraction of free fluids (unconfined phase).
744 ρ_{sc} is the volume-averaged density of the solids and confined fluids
745 \mathbf{u}_u is the velocity of the unconfined phase (free fluids)
746 \mathbf{u}_c is the velocity of the solids, confining solids and confined fluids
747 \mathbf{u}_s is the velocity of the solids
748 \mathbf{f} is the body force
749 \mathbf{M}_{DG} is the drag force
750 \mathbf{M}_{vm} is the virtual mass force
751 \mathbf{T}_c is the stress tensor for eh solids, confining solids and confined fluids
752 \mathbf{T}_u is the stress tensor for the free fluid phase
753 $\boldsymbol{\sigma}$ is the stress tensor
754 $\dot{\boldsymbol{s}}$ is the deviatoric shear stress rate tensor
755 δ is the Kronecker delta
756 $\dot{\boldsymbol{\epsilon}}_{plastic}$ is the plastic strain rate
757 $\dot{\boldsymbol{\epsilon}}_{elastic}$ is the elastic strain rate
758 λ is the plastic multiplier rate
759 g is the plastic potential function
760 $\dot{\boldsymbol{\epsilon}}_{total}$ is the total strain rate
761 $\dot{\boldsymbol{\epsilon}}$ is the deviatoric strain rate
762 ν is Poisson's ratio
763 E is the elastic Young's Modulus
764 G is the shear modulus
765 K is the Bulk elastic modulus
766 $f(I_1, J_2)$ is the yield surface, or yield criterion
767 $g(I_1, J_2)$ is the plastic potential function
768 ψ is the dilatancy angle
769 I_1 is the first stress invariant
770 J_2 is the second stress invariant
771 α_ϕ is the first Ducker-Prager material constant
772 k_c is the second Ducker-Prager material constant
773 $\dot{\boldsymbol{\omega}}$ is the spin rate tensor
774 ϵ_{v0} is the initial volumetric strain
775 ϵ_v is the volumetric strain
776 c_0 is the initial cohesion
777 $\boldsymbol{\tau}_f$ is the fluid Cauchy stress tensor
778 P_f is the fluid pressure
779 η_f is the fluids dynamic viscosity
780 \mathcal{A} is the mobility of the fluid at the interface
781 \mathcal{C}_{DG} is the drag coefficient
782 $U_{T,c}$ is the settling velocity of the solids, structured solids and confined fluids
783 $U_{T,uc}$ is the settling velocity of the unstructured solids
784 \mathcal{F} is the drag contribution from solid-like drag
785 \mathcal{G} is the drag contribution from fluid-like drag
786 \mathcal{S}_η is the smoothing function
787 \mathcal{K} is the absolute total mass flux

788 $M(Re_p)$ is an empirical function weakly dependent on the Reynolds number
 789 \mathcal{P} the partitioning parameter for the fluid and solid like contributions to drag
 790 m is an exponent for \mathcal{P}
 791 C_{VMG} is the virtual mass coefficient
 792 $|\mathbf{S}|$ is the norm of the shear force
 793 N is the normal force on a plane element
 794 g is the gravitational acceleration
 795 $P_{b,s,u}$ is the basal pressure from
 796 $P_{b,u}$ is the basal pressure from the free fluids
 797 $P_{b,c}$ is the basal pressure from the solids, structured solids and confined fluids
 798 \mathcal{B} is the pressure propagation factor for structured solids
 799 K_a is the active lateral earth pressure coefficient
 800 K_p is the passive lateral earth pressure coefficient
 801 ζ is a shape factor for the vertical gradient in solid concentration
 802 n is Mannings surface roughness coefficient
 803 X is the shape factor for the vertical fluid velocity profile
 804 Re_p is the particle Reynolds Number
 805 N_R is the Reynolds Number
 806 N_{RA} is the interfacial Reynolds Number
 807 H is the typical height of the flow
 808 L is the typical length of the flow
 809 α is the first viscosity parameter
 810 β the second viscosity parameter
 811 d is the grain diameter
 812 W is the kernel weight function
 813 r is the distance
 814 h is the kernel width (not to be confused with the flow height)
 815 q is the normalized particle distance
 816 Π_{ij} is an artificial viscosity term
 817 $F_{ij}^n R_{ij}^{\alpha\beta}$ is an artificial stress term
 818 ϵ_0 is a constant parameter for the artificial stress term
 819 α_Π and β_Π are constants in the artificial viscous force
 820 u_{sound} is the speed of sound in the material
 821 $N(\mathbf{x})$ is the Grid-kernel function
 822 c_p is the plastic coefficient
 823
 824
 825
 826
 827
 828
 829
 830

831 **Appendix B. Stress Remapping**

832 If, either due to degradation of strength parameters, or building numerical errors, the state of the stress
833 tensor lies beyond the yield surface, a correction must be applied. We implement the correction scheme used by
834 Bui et al. (2008). This scheme considers two primary ways in which the stress can have an undesired state:
835 Tension cracking, and imperfectly plastic stress.

836 **Tension Cracking**

837 In the case of tension cracking, the stress state has moved beyond the apex of the yield surface, as
838 described by Chen & Mizuno (1990). The employed solution in this case is to re-map the stress tensor along the
839 I_1 axis to be at this apex. The apex is provided by the yield function (Equation 89)

840 89. $-\alpha_\phi I_1 + k_c < 0$

841 To solve for this condition, the non-deviatoric stress state is increased (since $I_1 - \frac{k_c}{\alpha_\phi}$ is negative) to lie
842 perpendicular to the apex point on the I_1 axis (Equation).

843 90. $\bar{\sigma}^{\gamma\gamma} = r_S^{\gamma\gamma} - \frac{1}{3} \left(I_1 - \frac{k_c}{\alpha_\phi} \right)$

844 **Imperfect Plastic Stress**

845 Imperfect plastic stress described the state where the stress tensor lies above the apex, but beyond the
846 yield criterion, thus have more stress than supported by the failure criteria that is set. This criteria is simply the
847 yield surface itself (Equation 91).

848 91. $-\alpha_\phi I_1 + k_c < \sqrt{J_2}$

849 For this state, re-mapping is done by scaling of the J_2 value (Equations 92, 93 and 94).

850 92. $r = \frac{-\alpha_\phi I_1 + k_c}{\sqrt{J_2}}$

851 93. $\bar{\sigma}^{\gamma\gamma} = r_S^{\gamma\gamma} + \frac{1}{3} I_1$

852 94. $\bar{\sigma}^{xy} = r_S^{xy}, \bar{\sigma}^{xz} = r_S^{xz}, \bar{\sigma}^{yz} = r_S^{yz}$

853

854

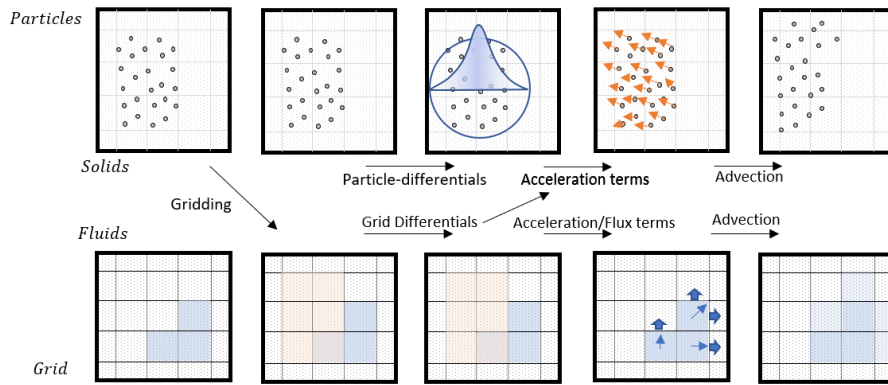
855

856 **Appendix C. Software Implementation**

857 The model presented in this article is part of the continued development of the OpenLISEM modelling
 858 tools. The most recent set of equations of implemented in the open-source alpha version of OpenLISEM Hazard
 859 2. Here, we describe the details of the implementation of the model into software.

860 **Hybrid MPM**

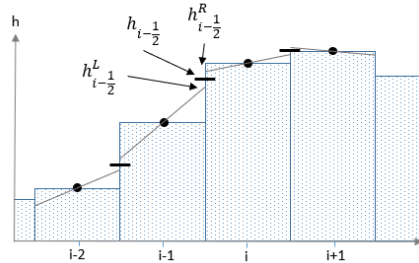
861 We utilize the MPM framework to be able to discretize part of the equations on a Eulerian regular grid,
 862 and part of the equations on the Lagrangian particles. Our distinct take on this method is the representation of the
 863 fluid phase completely as a finite element solution, while solids are simulated as discrete particle volumes. This
 864 allows the model to use the major benefits that are present when depth-averaged fluid flow is simulated in a grid.
 865 Both numerical efficiency, and high-accuracy coupling with hydrology are lacking in particle methods. For the
 866 solid phase, non-dissipative advection, fracturing and stiffness is a major benefit of the MPM approach. Since
 867 our model assumed confined fluids share their velocity with the solids, we advect the confined fluids as part of
 868 the particles. Total fluid volume is then calculated from the free fluids in the finite element data, and the gridded
 869 particle data. A flowchart of the software setup is provided in figure 6.



870
 871 *Figure 9 The sub-steps taken by the software to complete a single step of numerical integration.*

872 **Finite element solution**

873 We use a regular cartesian grid to describe the modelling domain. Terrain and cell-boundary based
 874 variables are re-produced using the MUSCL piecewise linear reconstruction (Delestre et al., 2014). For each cell-
 875 boundary, a left and right estimation of acceleration terms, velocity updates and new discharges is made. The left
 876 estimates use left-reconstructed variables while the other uses right-reconstructed variables. The final average
 877 flux through the boundary determines actual mass and momentum transfer. Local acceleration is averaged from
 878 the right estimate of the left boundary and left estimate of the right boundary. An additional benefit of the used
 879 scheme is the automatic estimation of continuous and discontinuous terrain. The piecewise linear reconstructions
 880 do not guarantee smooth terrain, for sharp locally variable terrain, pressure terms from vertical walls arise that
 881 block momentum. These terms allow for better estimation of momentum loss by barriers, but can be turned off if
 882 required for the simulated scenario.



883

884 *Figure 10 Piecewise linear reconstruction is used by the MUSCL scheme to estimate values of flow*
 885 *heights, velocities and terrain at cell-boundaries.*

886

GPU acceleration using OpenCL/OpenGL

887

888

889

890

891

892

893

894

895

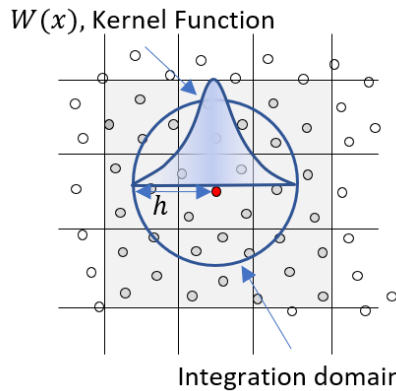
896

897

898

899

In order to create a more efficient setup, both the finite element and particle interactions are performed on the GPU. We utilize the OpenCL API to compile kernels written in c-style language. These kernels are compiled at the start of the simulation, and thereby allow for easy customization by users. While the usage of OpenCL 1.1 forces the usage of single precision floating point numbers, it allows for a wider range of GPU types to be supported. Finite element solutions on the GPU are straightforward, as maps are a basic data storage type for graphical processing units. Particles are stored as single-precision floating point arrays. Within the framework of MPM, iteration of particles within a kernel is required for each timestep and particle. This effectively means $O(n^2)$ operations are required. Significant efficiency improvements are obtained by pre-calculation sorting. Particles are sorted based on their location within the finite element grid. Based on the id of the gridcell, a bitonic mergesort is performed. This sorting algorithm works seamlessly on parallel architecture and operates as $O(n \log^2(n))$ (Batcher, 1968). Then, a raster is allocated to store the first indexed occurrence within the sorted list of particles of that gridcell. Since the kernel used for the presented work extends at most to a full width of two gridcells, we must iterate over all particles present in 9 neighboring grid cells.



900

901

902

903

901 *Figure 11 By limiting the kernel with and sorting particles before calculation, only the distance of*
 902 *particles in neighboring cells need to be checked, significantly reducing computational load, particularly for*
 903 *larger datasets.*

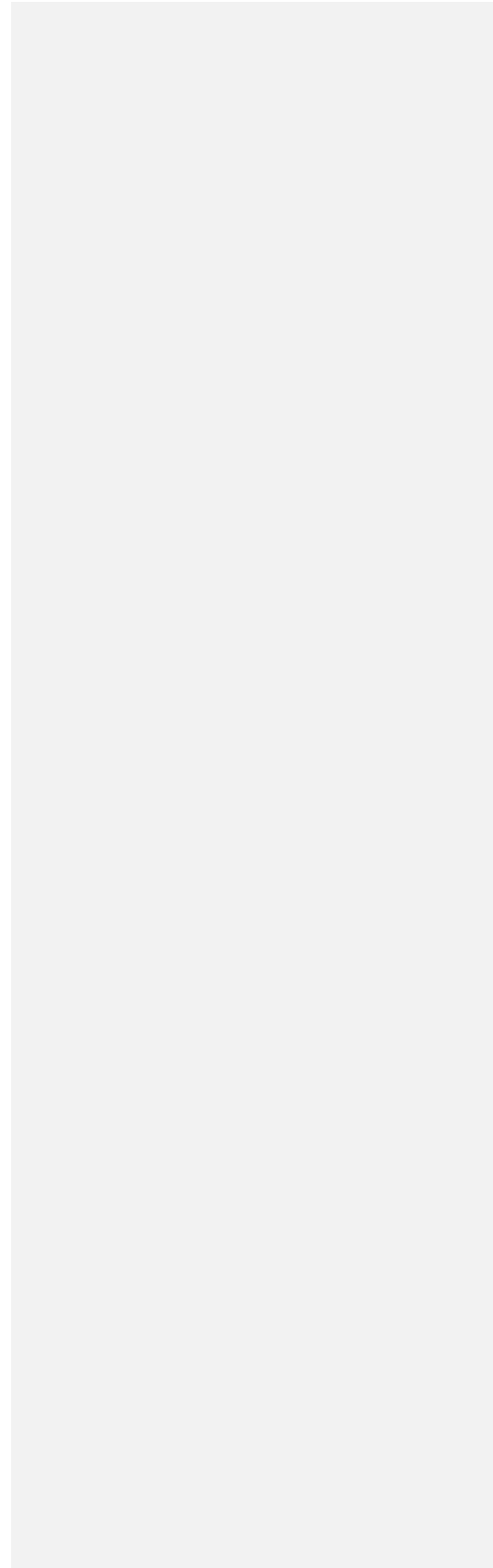
904

905

906

907

A final benefit to the usage of OpenCL is direct access to simulation variables for visualization in OpenGL using the OpenGL/OpenCL interoperability functionality. The built-in viewing window of OpenLISEM Hazard 2.0 alpha directly uses the data to draw both particles, shapefiles and grid data using customizable shaders written in the OpenGL shader language.



909

References

910

Aaron, J., & Hungr, O. (2016). Dynamic simulation of the motion of partially-coherent
911 landslides. *Engineering Geology*, 205, 1-11.

912

Abe, K., & Konagai, K. (2016). Numerical simulation for runoff process of debris flow using depth-
913 averaged material point method. *Soils and Foundations*, 56(5), 869-888.

914

Alsaman, M. E., Myers, M. T., & Sharf-Aldin, M. H. (2015, November). Comparison of multistage to
915 single stage triaxial tests. In *49th US Rock Mechanics/Geomechanics Symposium*. American Rock Mechanics
916 Association.

917

Bandara, S., Ferrari, A., & Laloui, L. (2016). Modelling landslides in unsaturated slopes subjected to
918 rainfall infiltration using material point method. *International Journal for Numerical and Analytical Methods in
919 Geomechanics*, 40(9), 1358-1380.

920

Batcher, K. E. (1968, April). Sorting networks and their applications. In *Proceedings of the April 30--
921 May 2, 1968, spring joint computer conference* (pp. 307-314).

922

Beutner, E. C., & Gerbi, G. P. (2005). Catastrophic emplacement of the Heart Mountain block slide,
923 Wyoming and Montana, USA. *Geological Society of America Bulletin*, 117(5-6), 724-735.

924

Bieniawski, Z. T. (1967, October). Mechanism of brittle fracture of rock: part I—theory of the fracture
925 process. In *International Journal of Rock Mechanics and Mining Sciences & Geomechanics Abstracts* (Vol. 4,
926 No. 4, pp. 395-406). Pergamon.

927

Bout, B., & Jetten, V. G. (2018). The validity of flow approximations when simulating catchment-
928 integrated flash floods. *Journal of hydrology*, 556, 674-688.

929

Bui, H. H., Fukagawa, R., Sako, K., & Ohno, S. (2008). Lagrangian meshfree particles method (SPH)
930 for large deformation and failure flows of geomaterial using elastic-plastic soil constitutive model. *International
931 journal for numerical and analytical methods in geomechanics*, 32(12), 1537-1570.

932

Chen, W. F., & Mizuno, E. (1990). *Nonlinear analysis in soil mechanics* (No. BOOK). Amsterdam:
933 Elsevier.

934

Cohen, D., Lehmann, P., & Or, D. (2009). Fiber bundle model for multiscale modeling of
935 hydromechanical triggering of shallow landslides. *Water resources research*, 45(10).

936

Corominas, J., Matas, G., & Ruiz-Carulla, R. (2019). Quantitative analysis of risk from fragmental
937 rockfalls. *Landslides*, 16(1), 5-21.

938

Corominas, J., van Westen, C., Frattini, P., Cascini, L., Malet, J. P., Fotopoulou, S., ... & Pitalakis, K.
939 (2014). Recommendations for the quantitative analysis of landslide risk. *Bulletin of engineering geology and the
940 environment*, 73(2), 209-263.

941

Cuomo, S., Pastor, M., Capobianco, V., & Cascini, L. (2016). Modelling the space-time evolution of
942 bed entrainment for flow-like landslides. *Engineering geology*, 212, 10-20.

943

DAVID, L. G., & RICHARD, M. (2011). A two-phase debris-flow model that includes coupled
944 evolution of volume fractions, granular dilatancy, and pore-fluid pressure. *Italian journal of engineering geology
945 and Environment*, 43, 415-424.

946

Davies, T. R., & McSaveney, M. J. (2009). The role of rock fragmentation in the motion of large
947 landslides. *Engineering Geology*, 109(1-2), 67-79.

948

Davies, T. R., McSaveney, M. J., & Beetham, R. D. (2006). Rapid block glides: slide-surface
949 fragmentation in New Zealand's Waikaremoana landslide. *Quarterly Journal of Engineering Geology and
950 Hydrogeology*, 39(2), 115-129.

951

De Vuyst, T., & Vignjevic, R. (2013). Total Lagrangian SPH modelling of necking and fracture in
952 electromagnetically driven rings. *International Journal of Fracture*, 180(1), 53-70.

953

Delaney, K. B., & Evans, S. G. (2014). The 1997 Mount Munday landslide (British Columbia) and the
954 behaviour of rock avalanches on glacier surfaces. *Landslides*, 11(6), 1019-1036.

955

Delestre, O., Cordier, S., Darboux, F., Du, M., James, F., Laguerre, C., ... & Planchon, O. (2014).
956 FullSWOF: A software for overland flow simulation. In *Advances in hydroinformatics* (pp. 221-231). Springer,
957 Singapore.

Formatted: English (United States)

Formatted: English (United States)

- 958 Dhanmeher, S. (2017). Crack pattern observations to finite element simulation: An exploratory study
959 for detailed assessment of reinforced concrete structures.
- 960 Drew, D. A. (1983). Mathematical modeling of two-phase flow. *Annual review of fluid*
961 *mechanics*, 15(1), 261-291.
- 962 Dufresne, A., Geertsema, M., Shugar, D. H., Koppes, M., Higman, B., Haeussler, P. J., ... & Gulick, S.
963 P. S. (2018). Sedimentology and geomorphology of a large tsunamigenic landslide, Taan Fiord,
964 Alaska. *Sedimentary Geology*, 364, 302-318.
- 965 Evans, S. G., Mugnozza, G. S., Strom, A. L., Hermanns, R. L., Ischuk, A., & Vinnichenko, S. (2006).
966 Landslides from massive rock slope failure and associated phenomena. In *Landslides from massive rock slope*
967 *failure* (pp. 03-52). Springer, Dordrecht.
- 968 Fornes, P., Bihs, H., Thakur, V. K. S., & Nordal, S. (2017). Implementation of non-Newtonian rheology
969 for Debris Flow simulation with REEF3D. IAHR World Congress.
- 970 Grady, D. E., & Kipp, M. E. (1980, June). Continuum modelling of explosive fracture in oil shale.
971 In *International Journal of Rock Mechanics and Mining Sciences & Geomechanics Abstracts* (Vol. 17, No. 3,
972 pp. 147-157). Pergamon.
- 973 Greco, M., Di Cristo, C., Iervolino, M., & Vacca, A. (2019). Numerical simulation of mud-flows
974 impacting structures. *Journal of Mountain Science*, 16(2), 364-382.
- 975 Griffiths, D. V., & Lane, P. A. (1999). Slope stability analysis by finite elements. *Geotechnique*, 49(3),
976 387-403.
- 977 Hayir, A. (2003). The effects of variable speeds of a submarine block slide on near-field tsunami
978 amplitudes. *Ocean engineering*, 30(18), 2329-2342.
- 979 Hušek, M., Kala, J., Hokeš, F., & Král, P. (2016). Influence of SPH regularity and parameters in
980 dynamic fracture phenomena. *Procedia engineering*, 161, 489-496.
- 981 Hutter, K., Svendsen, B., & Rickenmann, D. (1994). Debris flow modeling: A review. *Continuum*
982 *mechanics and thermodynamics*, 8(1), 1-35.
- 983 Ishii, M. (1975). Thermo-fluid dynamic theory of two-phase flow. *NASA Sti/recon Technical Report*
984 *A*, 75.
- 985 Ishii, M., & Zuber, N. (1979). Drag coefficient and relative velocity in bubbly, droplet or particulate
986 flows. *AIChE journal*, 25(5), 843-855.
- 987 Iverson, R. M. (2012). Elementary theory of bed-sediment entrainment by debris flows and
988 avalanches. *Journal of Geophysical Research: Earth Surface*, 117(F3).
- 989 Iverson, R. M., & Denlinger, R. P. (2001). Flow of variably fluidized granular masses across three-
990 dimensional terrain: 1. Coulomb mixture theory. *Journal of Geophysical Research: Solid Earth*, 106(B1), 537-
991 552.
- 992 Iverson, R. M., & Denlinger, R. P. (2001). Flow of variably fluidized granular masses across three-
993 dimensional terrain: 1. Coulomb mixture theory. *Journal of Geophysical Research: Solid Earth*, 106(B1), 537-
994 552.
- 995 Iverson, R. M., & George, D. L. (2014). A depth-averaged debris-flow model that includes the effects
996 of evolving dilatancy. I. Physical basis. *Proceedings of the Royal Society A: Mathematical, Physical and*
997 *Engineering Sciences*, 470(2170), 20130819.
- 998 Iverson, R. M., & Ouyang, C. (2015). Entrainment of bed material by Earth-surface mass flows: Review
999 and reformulation of depth-integrated theory. *Reviews of Geophysics*, 53(1), 27-58.
- 1000 Jakob, M., Hungr, O., & Jakob, D. M. (2005). *Debris-flow hazards and related phenomena* (Vol. 739).
1001 Berlin: Springer.
- 1002 Kaklauskas, G., & Ghaboussi, J. (2001). Stress-strain relations for cracked tensile concrete from RC
1003 beam tests. *Journal of Structural Engineering*, 127(1), 64-73.
- 1004 Kern, J. S. (1995). Evaluation of soil water retention models based on basic soil physical properties. *Soil*
1005 *Science Society of America Journal*, 59(4), 1134-1141.

- 1006 Kjekstad, O., & Highland, L. (2009). Economic and social impacts of landslides. In *Landslides—disaster*
1007 *risk reduction* (pp. 573-587). Springer, Berlin, Heidelberg.
- 1008 Li, C., Wang, C., & Qin, H. (2015). Novel adaptive SPH with geometric subdivision for brittle fracture
1009 animation of anisotropic materials. *The Visual Computer*, 31(6-8), 937-946.
- 1010 Libersky, L. D., & Petschek, A. G. (1991). Smooth particle hydrodynamics with strength of materials.
1011 In *Advances in the free-Lagrange method including contributions on adaptive gridding and the smooth particle*
1012 *hydrodynamics method* (pp. 248-257). Springer, Berlin, Heidelberg.
- 1013 Loehnert, S., & Mueller-Hoeppe, D. S. (2008). Multiscale methods for fracturing solids. In *IUTAM*
1014 *symposium on theoretical, computational and modelling aspects of inelastic media* (pp. 79-87). Springer,
1015 Dordrecht.
- 1016 Luna, B. Q., Remaître, A., Van Asch, T. W., Malet, J. P., & Van Westen, C. J. (2012). Analysis of
1017 debris flow behavior with a one dimensional run-out model incorporating entrainment. *Engineering*
1018 *geology*, 128, 63-75.
- 1019 Ma, G. W., Wang, Q. S., Yi, X. W., & Wang, X. J. (2014). A modified SPH method for dynamic failure
1020 simulation of heterogeneous material. *Mathematical Problems in Engineering*, 2014.
- 1021 Matsui, T., & San, K. C. (1992). Finite element slope stability analysis by shear strength reduction
1022 technique. *Soils and foundations*, 32(1), 59-70.
- 1023 Maurel, B., & Combescure, A. (2008). An SPH shell formulation for plasticity and fracture analysis in
1024 explicit dynamics. *International journal for numerical methods in engineering*, 76(7), 949-971.
- 1025 Menin, R. G., Trautwein, L. M., & Bittencourt, T. N. (2009). Smearred crack models for reinforced
1026 concrete beams by finite element method. *RIEM-IBRACON Structures and Materials Journal*, 2(2).
- 1027 Mergili, M., Frank, B., Fischer, J. T., Huggel, C., & Pudasaini, S. P. (2018). Computational experiments
1028 on the 1962 and 1970 landslide events at Huascarán (Peru) with r. avaflow: Lessons learned for predictive mass
1029 flow simulations. *Geomorphology*, 322, 15-28.
- 1030 Monaghan, J. J. (2000). SPH without a tensile instability. *Journal of computational physics*, 159(2),
1031 290-311.
- 1032 Nadim, F., Kjekstad, O., Peduzzi, P., Herold, C., & Jaedicke, C. (2006). Global landslide and avalanche
1033 hotspots. *Landslides*, 3(2), 159-173.
- 1034 Necas, J., & Hlaváček, I. (2017). *Mathematical theory of elastic and elasto-plastic bodies: an*
1035 *introduction*. Elsevier.
- 1036 Ngekpe, B. E., Ode, T., & Eluozo, S. N. (2016). Application of total-strain crack model in finite
1037 element analysis for punching shear at edge connection. *International journal of Research in Engineering and*
1038 *Social Sciences*, 6(12), 1-9.
- 1039 O'brien, J. S. (2007). FLO-2D users manual. *Nutr. Ariz. June*.
- 1040 O'brien, J. S., & Julien, P. Y. (1985). Physical properties and mechanics of hyperconcentrated sediment
1041 flows. *Proc. ASCE HD Delineation of landslides, flash flood and debris flow Hazards*.
- 1042 Osorno, M., & Steeb, H. (2017). Coupled SPH and Phase Field method for hydraulic
1043 fracturing. *PAMM*, 17(1), 533-534.
- 1044 Pailha, M., & Pouliquen, O. (2009). A two-phase flow description of the initiation of underwater
1045 granular avalanches. *Journal of Fluid Mechanics*, 633, 115-135.
- 1046 Pastor, M., Blanc, T., Haddad, B., Petrone, S., Morles, M. S., Drempetic, V., ... & Cuomo, S. (2014).
1047 Application of a SPH depth-integrated model to landslide run-out analysis. *Landslides*, 11(5), 793-812.
- 1048 Pastor, M., Blanc, T., Pastor, M. J., Sanchez, M., Haddad, B., Mira, P., ... & Drempetic, V. (2007). A
1049 SPH depth integrated model with pore pressure coupling for fast landslides and related phenomena. In *2007*
1050 *international forum on landslides disaster management* (pp. 987-1014).
- 1051 Pastor, M., Haddad, B., Sorbino, G., Cuomo, S., & Drempetic, V. (2009). A depth-integrated, coupled
1052 SPH model for flow-like landslides and related phenomena. *International Journal for numerical and analytical*
1053 *methods in geomechanics*, 33(2), 143-172.

Formatted: English (United States)

Formatted: Dutch (Netherlands)

1054 Pitman, E. B., & Le, L. (2005). A two-fluid model for avalanche and debris flows. *Philosophical*
1055 *Transactions of the Royal Society A: Mathematical, Physical and Engineering Sciences*, 363(1832), 1573-1601.

1056 Price, N. J. (2016). *Fault and joint development: in brittle and semi-brittle rock*. Elsevier.

1057 Pudasaini, S. P. (2012). A general two-phase debris flow model. *Journal of Geophysical Research:*
1058 *Earth Surface*, 117(F3).

1059 Pudasaini, S. P., & Fischer, J. T. (2016). A mechanical erosion model for two-phase mass flows. *arXiv*
1060 *preprint arXiv:1610.01806*.

1061 Pudasaini, S. P., & Hutter, K. (2003). Rapid shear flows of dry granular masses down curved and
1062 twisted channels. *Journal of Fluid Mechanics*, 495, 193-208.

1063 Pudasaini, S. P., & Hutter, K. (2007). *Avalanche dynamics: dynamics of rapid flows of dense granular*
1064 *avalanches*. Springer Science & Business Media.

1065 Pudasaini, S. P., & Mergili, M. (2019). A Multi-Phase Mass Flow Model. *Journal of Geophysical*
1066 *Research: Earth Surface*.

1067 Pudasaini, S. P., Hajra, S. G., Kandel, S., & Khattri, K. B. (2018). Analytical solutions to a nonlinear
1068 diffusion–advection equation. *Zeitschrift für angewandte Mathematik und Physik*, 69(6), 150.

1069 Reiche, P. (1937). The Toreva-Block: A distinctive landslide type. *The Journal of Geology*, 45(5), 538-
1070 548. Richard, A., Brennan, G., Oh, W. T., & Heme, V. (2017). Critical height of an unsupported vertical trench in
1071 an unsaturated sand. In *Proceedings of the 70th Canadian Geotechnical Conference*.

1072 Rickenmann, D., Laigle, D. M. B. W., McArdell, B. W., & Hübl, J. (2006). Comparison of 2D debris-
1073 flow simulation models with field events. *Computational Geosciences*, 10(2), 241-264.

1074 Roberts, M., <http://extremelearning.com.au/evenly-distributing-points-in-a-triangle/> Obtained 29-01-
1075 2020

1076 Savage, S. B., & Hutter, K. (1989). The motion of a finite mass of granular material down a rough
1077 incline. *Journal of fluid mechanics*, 199, 177-215.

1078 Saxton, K. E., & Rawls, W. J. (2006). Soil water characteristic estimates by texture and organic matter
1079 for hydrologic solutions. *Soil science society of America Journal*, 70(5), 1569-1578.

1080 Sheridan, M. F., Stinton, A. J., Patra, A., Pitman, E. B., Bauer, A., & Nichita, C. C. (2005). Evaluating
1081 Titan2D mass-flow model using the 1963 Little Tahoma peak avalanches, Mount Rainier, Washington. *Journal*
1082 *of Volcanology and Geothermal Research*, 139(1-2), 89-102.

1083 Stead, D., & Wolter, A. (2015). A critical review of rock slope failure mechanisms: The importance of
1084 structural geology. *Journal of Structural Geology*, 74, 1-23.

1085 Steffen, M., Kirby, R. M., & Berzins, M. (2008). Analysis and reduction of quadrature errors in the
1086 material point method (MPM). *International journal for numerical methods in engineering*, 76(6), 922-948.

1087 Sticko, S. (2013). Smooth Particle Hydrodynamics applied to fracture mechanics.

1088 Stomakhin, A., Schroeder, C., Chai, L., Teran, J., & Selle, A. (2013). A material point method for snow
1089 simulation. *ACM Transactions on Graphics (TOG)*, 32(4), 1-10.

1090 Tang, C. L., Hu, J. C., Lin, M. L., Angelier, J., Lu, C. Y., Chan, Y. C., & Chu, H. T. (2009). The
1091 Tsaoling landslide triggered by the Chi-Chi earthquake, Taiwan: insights from a discrete element
1092 simulation. *Engineering Geology*, 106(1-2), 1-19.

1093 Van Asch, T. W., Tang, C., Alkema, D., Zhu, J., & Zhou, W. (2014). An integrated model to assess
1094 critical rainfall thresholds for run-out distances of debris flows. *Natural hazards*, 70(1), 299-311.

1095 Van Looy, K., Bouma, J., Herbst, M., Koestel, J., Minasny, B., Mishra, U., ... & Schaap, M. G. (2017).
1096 Pedotransfer functions in Earth system science: Challenges and perspectives. *Reviews of Geophysics*, 55(4),
1097 1199-1256.

1098 Varnes, D. J. (1978). Slope movement types and processes. *Special report*, 176, 11-33.

1099 von Boetticher, A., Turowski, J. M., McArdell, B. W., Rickenmann, D., & Kirchner, J. W. (2016).
1100 DebrisInterMixing-2.3: a finite volume solver for three-dimensional debris-flow simulations with two calibration
1101 parameters-Part I: Model description. *Geoscientific Model Development*, 9(9), 2909-2923.

- 1102 Williams, J. R. (2019, October). Application of SPH to coupled fluid-solid problems in the petroleum
1103 industry. In *Videos of Plenary Lectures presented at the IV International Conference on Particle-Based*
1104 *Methods. Fundamentals and Applications.(PARTICLES 2015)*.
- 1105 Xie, M., Esaki, T., & Cai, M. (2006). GIS-based implementation of three-dimensional limit equilibrium
1106 approach of slope stability. *Journal of geotechnical and geoenvironmental engineering*, 132(5), 656-660.
- 1107 Xu, F., Zhao, Y., Li, Y., & Kikuchi, M. (2010). Study of numerical and physical fracture with SPH
1108 method. *Acta Mechanica Solida Sinica*, 23(1), 49-56.
- 1109 Zhang, L. L., Zhang, J., Zhang, L. M., & Tang, W. H. (2011). Stability analysis of rainfall-induced
1110 slope failure: a review. *Proceedings of the Institution of Civil Engineers-Geotechnical Engineering*, 164(5), 299-
1111 316.
- 1112 Zhou, F., Molinari, J. F., & Ramesh, K. T. (2005). A cohesive model based fragmentation analysis:
1113 effects of strain rate and initial defects distribution. *International Journal of Solids and Structures*, 42(18-19),
1114 5181-5207.